atmosphere

MDPI

Article

Northern Hemisphere Seasonal Cycle of Explosive Growth and Decay of Storms

Jorgen S. Frederiksen [1,*] and Stacey L. Osbrough [2]

[1] School of Geography, Earth and Atmospheric Sciences, University of Melbourne, Melbourne, VIC 3010, Australia
[2] CSIRO Environment, Aspendale, Melbourne, VIC 3195, Australia; stacey.osbrough@csiro.au
* Correspondence: jorgen.frederiksen@unimelb.edu.au

Abstract

The statistics of the growth and decay of Northern Hemisphere (NH) synoptic-scale weather systems are determined for each season during the 20 years between 1997 and 2016. Six hourly reanalysis data are spectrally analyzed in space and time and studied in a high-pass (periods < 4 days) and band-pass (periods between 4 and 8 days) frequency band and in three growth rate and three decay rate bins. Leading Empirical Orthogonal Functions (EOFs) and storm tracks based on 850 hPa meridional winds and streamfunctions are determined for each frequency band and each growth rate bin and compared with standard EOFs and storm tracks based on all (growing and decaying) disturbances. Leading standard EOFs and EOFs associated with slow growth rates have peak amplitudes across the Pacific and North America–Atlantic sectors between 40° N and 60° N in both frequency bands. For moderate and explosive growth rates, there are equatorward shifts in the peak amplitudes of the leading EOFs, which are reflected in the variance of streamfunctions. Through the seasonal cycle, and for both bands and all growth rate bins, the variance of synoptic-scale disturbances have peaks over the main Pacific and North American–Atlantic sectors with extensions across Europe and Siberia. Explosive storms contribute to activity over the Mediterranean and North Africa and across the Middle East, India and China depending on season and periods.

Keywords: storm tracks; cyclogenesis; growth rates; seasonal variability

1. Introduction

Extratropical storms are key drivers of weather and climate. These westward tilting cyclones, which constitute the low-pressure component of eastward propagating Rossby wavetrains [1,2], transport heat and momentum and moisture. They are initiated by baroclinic instability and enhanced by latent heat release, primarily in the tropospheric jet streams in both hemispheres. The frontal model marked the beginning of a mechanistic scientific understanding of storm formation. It was developed more than a hundred years ago by the Bergen School led by J. Bjerknes [3,4]. In the mid-20th century came the paradigm shift in understanding with the mathematical theory of baroclinic instability for extratropical cyclogenesis by Charney [5], Eady [6] and Phillips [7]. With this underpinning, the subsequent advances in weather prediction and understanding of synoptic weather systems have been rapid and impressive.

Check for updates

Academic Editor: Tomeu Rigo

Received: 17 March 2026
Revised: 8 May 2026
Accepted: 8 May 2026
Published: 14 May 2026

Copyright: © 2026 by the authors. Licensee MDPI, Basel, Switzerland. This article is an open access article distributed under the terms and conditions of the Creative Commons Attribution (CC BY) license.

1.1. Storm Tracks from Eulerian Variance of Weather Fluctuations

The observational study of NH high- and low-frequency atmospheric fluctuations by Sawyer [8] was one of the earliest works where storm tracks were depicted as the regions of high standard deviation (STD) of the 500 hPa geopotential height. His Figure 5 shows the clear Atlantic storm track and the north-west part of the Pacific storm track, based on the high-pass anomaly of the 11-day running mean of British Meteorological Office daily data for the 3-year time interval 1961 to 1963.

More detailed analyses of high-pass, band-pass and low-pass filtered twice daily NH winter and summer 500 hPa geopotential height fields, for the time interval 1963 to 1972, were made by Blackmon [9]. The band-pass winter STDs of US national Meteorological Center (NMC) data, with periods between 2.5 and 6 days, in Blackmon's Figure 5a capture the locations of both the Atlantic and Pacific storm tracks, with centers slightly downstream and poleward of the regions of maximum jet strengths and baroclinicity. This is also the case for summer as shown in Blackmon's Figure 9a. As noted there, the summer maxima are reduced compared with winter, and the summer peak of the Atlantic storm track is located to the north of the winter maximum.

Blackmon, et al. [10] expanded on his 1976 work by examining multiple fields of the twice-daily NH winter circulation again between 1963 to 1972. These included sea-level pressure and 300 hPa height, as well as 500 hPa zonal and meridional winds, 850 hPa temperature and poleward heat flux. They determined that the STDs at the surface and 500 and 300 hPa were quite similar for both band-pass and low-pass filtered data with increases of circa 1.7 in geopotential height fluctuations between the sea level and 300 hPa. Also noteworthy are the broad similarities between the storm tracks represented by the 500 hPa meridional wind in Figure 5b of Ref. [10] and the geopotential height in Figure 5a of Ref. [9].

In the half century since these earliest studies of storm tracks based on the STDs of synoptic-scale fluctuations, the number and quality of atmospheric data sets have significantly advanced. With this, our detailed knowledge of the properties of weather systems has increased, through a wide range of data-analysis studies and theoretical studies on their genesis. The Eulerian approach of describing storm tracks by the STDs or variance of synoptic-scale fluctuations has played a dominant role in subsequent works. Following the articles of Blackmon, there was a flurry of activity to analyze the three-dimensional structures of the NH storm track and associated transient eddy fluxes and their relationships to the large-scale flow fields. Lau and collaborators [11–14] made detailed studies of the NH winter transients with both US NMC and Geophysical Fluid Dynamics Laboratory (GFDL) circulation data. White [15] made related studies of NH summer synoptic-scale fluctuations and compared the results for the two seasons.

Thereafter, there followed many subsequent studies of the transient eddy statistics of the NH based on the Eulerian variances or STDs. Of particular interest for this article are the works of Wallace, et al. [16], Nakamura [17], Chang and Yu [18], Chang [19] and Hoskins and Hodges [20]. Wallace, et al. [16] analyzed the propagation characteristics of NH Rossby wavetrains of synoptic-scale weather systems and determined their structures through key point correlation and lagged correlation analysis. They considered twenty winters of NMC data between 1964 and 1984.

Nakamura [17] studied the mid-winter suppression of the baroclinic transients in the Pacific in a data-analysis study and related the results to the strength of the upper-tropospheric zonal mean flow. Chang and Yu [18] examined the statistical wavetrain structure of the synoptic-scale transiens in the NH winter through one-point lag correlation maps and based on the European Centre for Medium-Range Weather Forecasting (ECMWF)

reanalysis data [21] for the period 1980 to 1993. Chang [19] extended the study to also consider SH wavetrains and to both the summer and winter seasons in each hemisphere.

Hoskins and Hodges [20] made detailed analyses of the NH winter storm tracks and eddy statistics based on both Eulerian STDs and Lagrangian tracking methods using three reanalysis data sets. These were reanalyses from ECMWF [21], the National Centers for Environmental Prediction and National Center for Atmospheric Research (hereafter NNR) [22] and Goddard Earth Observing System 1 (GEOS-1) [23]. They found generally very good agreement between the results of their Eulerian and Lagrangian tracking methods and showed the robustness of the results based on different reanalyses including the early works going back to Blackmon and collaborators [9,10]. As reviewed by Osbrough and Frederiksen [24], the Eulerian approach has also been extensively applied in the study of Southern Hemisphere (SH) storm tracks [19,25–32].

1.2. Storm Tracks from Lagrangian Tracking Methods

The earliest method of characterizing storm tracks, going back to the late 19th century, consisted of manual identification and Lagrangian tracking of the paths of weather systems and the compositing of the cyclone tracks to form the requisite statistics (e.g., Klein [33]). With the forecast based on numerical prediction, the Eulerian method of calculating variances or STDs became a more popular direct method of determining storm tracks and eddy statistics. The Lagrangian method has come back into favor, for studies of circulation statistics in both hemispheres, with the development of automatic tracking algorithms since the late 20th century [34–50].

Lagrangian tracking methods have also been used to establish global climatologies of explosive cyclogenesis (e.g., Allen, et al. [51]). As emphasized by several authors [20,43], the results based on Lagrangian tracking methods do depend on choices and constraints imposed, such as on the track continuity and smoothness. These choices can be important for obtaining consistency between Lagrangian and Eulerian methods. For example, Sinclair [43] found that requiring weather systems to move by 10° during their evolution led to cyclone track densities that were in much better agreement with Eulerian statistics for the four seasons of the SH. Similar requirements were made by Hoskins and Hodges [20,45] and led to close agreement between their Eulerian and Lagrangian results for both hemispheres.

1.3. Data-Driven Determination of Growing and Decaying Weather Systems

The standard Eulerian and Lagrangian tracking methods are somewhat complementary and, together with model simulations and theoretical models and insights, highlight different aspects of the complexity of storm tracks. The data-driven method of Osbrough and Frederiksen [24,52,53] extends the Eulerian approach to calculate the separate contributions to the statistics of weather systems in different growth rate and decay rate bins. In this sense, it combines some of the instability aspects of the theoretical models and Lagrangian tracking with the Eulerian approach for determining intensity. Like the standard Eulerian method, one specifies the frequency bands of interest. However, there are no further assumptions about the movement or lifetime of the disturbances, but growth and propagation effects are separated. It avoids the possibility of the apparent deepening of cyclones through rapid movement into regions of climatological low pressure that can occur with Lagrangian tracking methods [44,54].

The method of Refs. [24,52,53] also provides clarity on the changes in storms that occur due to changing climate, which may not be evident from the standard Eulerian method based on all fluctuations in a given frequency band. Osbrough and Frederiksen [53] provide examples where reductions and shifts in explosive storms between decades and multiple decades are somewhat compensated by changes in slower growing disturbances. Thus,

the changes that occur can, to a significant extent, be a replacement of explosive storms by slower growing storms, as well as some latitudinal shifts [53,55,56]. Their method provides yet another complementary way of studying atmospheric disturbances.

1.4. Explosive Storms, Latent Heat Release and Tropical-Extratropical Interactions

The works of Osbrough and Frederiksen [52,53], while analyzing disturbances in several growth rate and decay rate bins, had emphasis on explosive storms. This was because it was found that Southern Australia rainfall changes were most related to changes in the fast growing storms. Of course it has long been known that rainfall is associated with circulations with strong ascending motion [4]. As well, there have been many diagnostic and Lagrangian tracking studies of extratropical cyclones that have found that the rate of deepening is strongly correlated with rainfall (Refs. [57–66] and our Appendices A and B). In both the NH and SH, heavy downpours tend to occur during explosive cyclogenesis.

As noted in Refs. [52,53] diabatic effects play important roles in extratropical storm development in the SH such as through imbedded thunderstorms and for north-west cloud band disturbances and east coast lows, which can develop from tropical cyclones. In the NH, the relative roles of baroclinic instability, diabatic processes and tropical–extratropical interactions on cyclone development are arguably even more complex as summarized in our Appendices A and B.

1.5. Aims and Structure of Article

Our primary aims are to further advance research into the seasonal variability of NH synoptic-scale weather systems in the following ways:

A. We use streamfunction Ψ, rather than geopotential height, and $cos\phi$ weighted meridional wind, $V = vcos\phi = a^{-1}\partial\Psi/\partial\lambda$. Here v is the nondivergent meridional wind, a is the radius of the Earth, λ is the longitude and ϕ is the latitude. This allows a clearer determination of the roles of synoptic-scale disturbances in the subtropics, as well as in the extratropics.
B. We examine weather systems in both high-pass (periods $T_r < 4$) and band-pass (periods $4 \leq T_r < 8$) bands. This allows insights into dipole onset-of-blocking disturbances in the band-pass band and largely high-pass band disturbances of the subtropics, as well as the relative roles of the two bands in the main extratropical storm tracks.
C. We present our findings for disturbances in three growth rate bins and three decay rate bins, as well as results for the combined fluctuations and for both bands. The regions of preferential growth of explosive extratropical cyclones are analyzed, as well as the impacts of more slowly growing and decaying disturbances.

The specific goals of this article are to study the NH seasonal variations in the following:

1. The relationships between the large-scale flows, particularly the zonal winds, and the structures and variability of synoptic-scale fluctuations.
2. The 'standard' EOFs for all 850 hPa $cos\phi$ weighted meridional wind transients in both frequency bands.
3. The 'instability' EOFs based on filtered 850 hPa $cos\phi$ weighted meridional winds anomalies in three growth rates, ϖ_i, bins with $0 \leq \varpi_i < 0.5$ day^{-1}, $0.5 \leq \varpi_i < 1.0$ day^{-1} and $\varpi_i \geq 1.0$ day^{-1}.
4. The storm tracks determined by the STDs of all filtered 850 hPa streamfunction transients for high-pass and band-pass data.
5. The storm tracks from STDs of growing and decaying filtered 850 hPa streamfunction fluctuations in three growth rate and three decay rate bins.

6. The relationships between synoptic-scale weather systems and their statistics in different growth rate bins and frequency bands and the likely influences of moist processes and tropical–extratropical interactions.
7. NNR 6-hourly data during the 20-year time span 1997 to 2016. This will also form the baseline for a sequel in which interdecadal changes in weather systems over the last 70 years are examined.

The plan of the article is as follows. The 6-hourly NNR reanalysis data set that we examine in this work is described in Section 2. The method that we use for determining growing and decaying weather systems directly from the reanalysis data and to filter the flow fields into high-pass and band-pass components is described in Section 3. There we also document the growth rate ranges of the three growth and three decay rate bins that are employed throughout this article. As well, the 'instability' EOFs, characterizing the anomalies in different growth rate bins, and the 'standard' EOFs, based on all growing and decaying filtered disturbances, are discussed in Section 3.

The outcomes of our study are documented in Sections 4–8. Section 4 presents the seasonal cycle of the 300 hPa and 700 hPa NH zonal winds averaged for the 20-year period between 1997 to 2016. The standard EOFs, based on all 850 hPa meridional wind fluctuations in the two frequency bands, are depicted in Section 5. Their seasonal variability is noted for both the leading monopole wavetrains and for band-pass subdominant dipole structures indicative of the onset of blocking [67,68]. Associated instability EOFs for growing weather systems in three growth rate bins are presented in Section 6 and compared with related standard EOFs. The seasonal cycle of the standard NH storm tracks, based on STDs of 850 hPa SH streamfunction for all fluctuations in each band, is analyzed in Section 7. The corresponding storm tracks for the separate contributions of growing and decaying disturbances in three growth and three decay rate bins are presented in Section 8.

The implications of our findings and our conclusions are summarized in Section 9. Appendix A contains a summary of theories and modeling of extratropical storm tracks and comparisons between theories and observational results on the climatology of storm tracks. Appendix B contains a summary of the diversity of cyclones and their classification, on tropical–extratropical transitions, on the roles of diabatic process in the development of storms and on synoptic-scale weather systems of different geographical regions. Our methodology for extracting growing and decaying disturbances from 6-hourly reanalysis data and calculating their growth rates is presented in Appendix C. The method for determining EOFs is documented in Appendix D and Appendix E contains a description of the Phillips' criterion for incipient baroclinic instability.

2. Datasets

One of the aims of this study is to examine the extent to which the broad principles established in our studies of SH weather systems [24,52,53] also extend to NH disturbances. For that we shall again perform the analyses over the time interval 1997 to 2016 and use the 'Reanalysis 1' dataset from the National Centers for Environmental Prediction (NCEP) and the National Centre for Atmospheric Research (NCAR) [22]. Hereafter, we shall refer to it as NNR. The resolution of NNR is 2.5° latitude by 2.5° longitude, which is more than adequate for our rhomboidal 31 (*R*31) study. It was chosen because it is available for more than seven decades going back to 1948 and so is suitable for examining circulation changes over an extensive time interval. Moreover, as reviewed in Refs. [53,69,70], it has broad consistency with station data and dynamical consistency with independent Australian rainfall changes even in the early periods.

We again use the 6-hourly meteorological fields from the NNR data with a focus on the $cos\phi$ weighted meridional winds and on flow fields for constructing the streamfunction. In

our analysis, we examine a considerable larger set of diagnostics than conventional studies with two frequency bands and six growth rate bins, as well as standard diagnostics. For that reason, we focus on the 850 hPa level, which, in the study of Osbrough and Frederiksen [53], was found to be most related to extratropical rainfall changes. In this article, we present NH results for the 20-year time interval 1997 to 2016; this is also the time period analyzed in the related SH study in Ref. [24]. We present our results for the four seasons of winter (DJF), autumn (SON), summer (JJA) and spring (MAM) or for central months in each season. In a future article, we plan to examine the interdecadal variability in statistics of NH weather systems since the mid-20th century.

3. Method for Determining Growing and Decaying Weather Systems

The 6-hourly NNR data described in Section 2 is spectrally analyzed in terms of spherical harmonics. We focus on the $cos\phi$ weighted meridional wind and the streamfunction, which is obtained from the zonal and meridional winds. For example, the streamfunction is represented by the following:

$$\Psi(\lambda, \mu, t) = \sum_m \sum_n \Psi_{mn}(t) P_n^m(\mu) e^{im\lambda}. \quad (1)$$

Here, $P_n^m(\mu)$ are Legendre functions dependent on zonal (m) and total (n) wavenumbers and on $\mu = sin\phi$, the sine of the latitude (ϕ). The longitudinal dependence is represented by the Fourier term $e^{im\lambda}$ with λ the longitude. Since the physical space streamfunction and meridional fields are real, the spectral coefficients Ψ_{mn} must have the property that $\Psi_{-mn}(t) = \Psi_{mn}^*(t)$. Throughout this article we use a resolution of rhomboidal 31 ($R31$) for which m ranges from -31 to 31 and n from $n = |m|$ to $|m| + 31$. In physical space, $R31$ corresponds to a resolution of approximately 250 km in latitude and 300 km in longitude at 45° N.

In a corresponding study on SH extratropical synoptic-scale weather systems, Osbrough and Frederiksen [53] found that $R31$ was more than sufficient for determining the leading EOFs and standard deviations of streamfunctions. Indeed, they found that using even an $R15$ resolution left their presented results and conclusions essentially unchanged. This is a consequence of the fact that transient kinetic energy spectra fall off rapidly with essentially -3 power laws at the smaller scales [71]. This in turn is reflected in the leading EOFs, which explain the larger proportions of the variance and in the standard deviations of streamfunction fluctuations. These results are also consistent with traditional baroclinic instability theory [54]. The radius of extratropical cyclones, estimated from data analysis, can be relatively small for some disturbances, dependent somewhat on the methodology [54,72]. Nielsen and Dole [54], however, note that most cyclones with a radius of 300 km or less are stationary, their travelling cyclones have a mean radius of 875 km, and their "normal" or "prominent" cyclones, of substantial intensity, have an average radius of 1500 km (wavelength of 3000 km).

Osbrough and Frederiksen [53] developed a method for determining the statistics of growing and decaying weather systems in different growth rate bins, as well as in different frequency bands, which is used here. Firstly, the anomalies with respect to the climatological annual cycle are determined and spectrally analyzed. The fluctuations are then separated into two bands of high-pass ($T_r < 4$ days) and band-pass ($4 \leq T_r < 8$ days) filtered components where T_r is the period. A filter length of $K = 40$, as defined in Appendix 2 of Ref. [53], was found to be near optimal and is used here. Our Appendix C gives a summary of how the separate growing and decaying components and their growth rates are obtained.

The weather systems are then composited into the six growth rate bins shown in Table 1, and the leading EOFs are calculated as described in Appendix D. With the current resolution of rhomboidal 31, this results in large eigenvalue problems with 2460 EOFs. The standard deviations (STDs) of the disturbances and the EOFs are analyzed for each band and for both the six growth rate bins ('instability' EOFs) and for all (growing and decaying) components in each band ('standard' EOFs). In fact, we shall focus on the EOFs corresponding to growing disturbances, as well as the standard EOFs, but present all STDs.

Table 1. Bin numbers and growth rate ranges of the six growth rate bins.

Bin Number	Growth Rate Bins
(i)	$\varpi_i < -1$ day^{-1}
(ii)	-1 day$^{-1} \leq \varpi_i < -0.5$ day^{-1}
(iii)	-0.5 day$^{-1} \leq \varpi_i < 0$ day^{-1}
(iv)	0 day$^{-1} \leq \varpi_i < 0.5$ day^{-1}
(v)	0.5 day$^{-1} \leq \varpi_i < 1$ day^{-1}
(vi)	$\varpi_i \geq 1$ day^{-1}

4. Seasonal Cycle of Northern Hemisphere Zonal Winds

The zonal winds of both hemispheres are focused in several westerly extratropical jet streams and with easterlies largely in the near equatorial regions. The westerly jets are located at mid latitudes at the descending branch of the Hadley circulation. Figure 1 shows the structure of the NH climatological zonal winds, for 1997 to 2016, in each season and at the 700 hPa and 300 hPa levels. Very evident are the dominant extratropical westerly jets extending from East Asia across the Pacific Ocean and from the east coast of North America across the Atlantic Ocean with peak strengths between 30° N and 45° N. As well, a somewhat weaker jet stream extends across the Middle East and Asia with peak strength near 30° N. In the warm season of JJA, and particularly at 300 hPa, the Pacific and Atlantic jets are relatively weaker, and the three jets essentially join up and extend across most of the NH extratropics. The subtropical jets have larger peaks at 300 hPa compared with 700 hPa and are strong and deep throughout the seasonal cycle but with reduced amplitudes in boreal summer.

In the following sections, we calculate and analyze, in detail, the properties of weather systems based on the methods described in Section 3 and Appendices C and D and relate their characteristics to the jetstreams. However, a simple criterion that provides broad guidance to the likely regions of baroclinic instability and storm formation is Phillips' [7] criterion described in Appendix E. As noted there, the condition for incipient baroclinic instability occurs when the vertical shear of the zonal wind between appropriate vertical level exceeds a critical value.

We note that the difference in the 300 hPa zonal wind minus that at 700 hPa is an estimate of the mid-tropospheric baroclinicity, while the 700 hPa zonal wind can also be regarded as a measure of the lower tropospheric baroclinicity since the surface winds are relatively weak. In fact, it has been found [53,69] that 700 hPa zonal wind changes have strong correlations with changes in Southern Australian cool season rainfall.

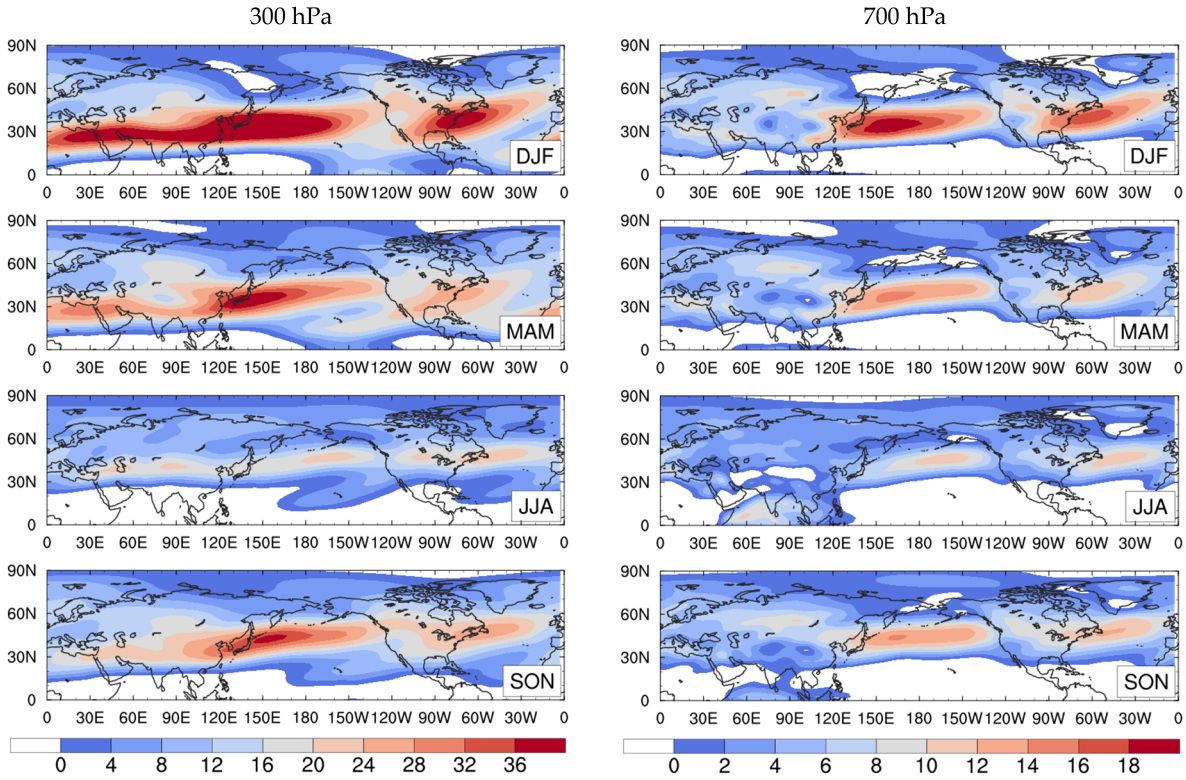

Figure 1. Northern Hemisphere climatological zonal winds at (**a**) 300 hPa and (**b**) 700 hPa for 1997 to 2016 in each season DJF, MAM, JJA and SON.

The structures of the NH jet streams shown in Figure 1 are also seen in other long-time averages of zonal winds over the last 70 years. However, there have been systematic shifts with time, as in the SH [52], that will be examined in a sequel to this article.

5. Standard EOFs—All Fluctuations

In this Section, we analyze the structures of leading NH synoptic-scale weather systems, particularly monopole Rossby wavetrains of high and low pressure in the main storm tracks, and of dipole onset-of-blocking modes [67,68], in each case represented by their EOFs. As in the studies of Refs. [24,52,53], our focus is on EOFs, calculated as described in Appendix D, since they are relatively easily generalized to 'instability' EOFs. These instability modes are considered in subsequent sections and are based on separate fluctuations in different growth rate and decay rate bins. This contrasts with Principal Oscillation Patterns (POPs), which need to be based on the stationary statistics of all growing and decaying disturbances in the standard formulations. Nevertheless, as discussed by Osbrough and Frederiksen [53], travelling modes described by POPs can often be associated with essentially a pair of phase-shifted EOFs.

The EOFs considered in this Section are the so-called 'standard' EOFs determined from all growing and decaying disturbances in given frequency bands. We consider two bands of high-pass (T_r $<$ 4 days) and band-pass (4 $\leq$ T_r $<$ 8 days) disturbances as in our SH studies [24,52,53].

The EOFs provide a complete basis for representing any local synoptic-scale disturbance, and thus, many EOFs with similar contributions to the variance explained will in general be needed to represent it. As a consequence, the variance explained with an increasing mode number falls off slower than for large scale disturbances such as the Madden Julian Oscillation [73,74], where the first two EOFs of outgoing longwave radiation

variability explain 11% and 10% of the variance, respectively, falling off to 5% for EOF3 [73]. For the current synoptic-scale disturbances, the first EOF1 typically explains about half of these values, at around 5%, falling off to roughly 1% at EOF20 and 0.2% at EOF100. For example, for the January cases considered in Sections 5.1 and 5.2 below, EOF numbers (1, 20, 100) explain respectively (4.4, 0.9, 0.2) % of the variance for high-pass disturbances and (6.6, 1.1, 0.2) % of the variance for band-pass disturbances. Again, dominant larger scale modes capture more of the variance.

In the following Section 6, we then calculate and analyze 'instability' EOFs for these same frequency bands and in six bins (Table 1) of growing and decaying weather systems. Again, throughout this article, our EOFs are derived from 6-hourly data of meridional wind anomalies ($cos\phi$ weighted) with a focus on the associated 850 hPa streamfunction fields. Our choice is based on making comparisons with the SH results of Refs. [24,52,53] and on the fact that there it was found that variability at the 850 hPa level was most related to extratropical rainfall variability.

We focus on a few of the leading EOFs, which generally have large amplitudes in the main Pacific or North American–Atlantic storm tracks, or both, and in some cases in other regions. EOFs for transient disturbances often occur in related phase-shifted pairs of which we only consider one. The Supplement provides further examples of the diversity of the EOFs.

We analyze the EOFs in the central months of the seasons starting in boreal winter (January) followed in sequence by spring (April), summer (July) and autumn (October). This again is a convenient order since in both hemispheres extratropical storminess tends to be particularly strong during the cooler seasons [24]. Again, the EOFs for the central months are generally typical of the associated seasons.

5.1. High-Pass Filtered Weather Systems with Periods $T_r < 4$ Days

Figure 2a shows the 850 hPa streamfunction for the dominant January meridional wind EOF1. It is a wavetrain with a monopole structure in the latitudinal direction located at the latitudes of the 700 hPa winter zonal wind shown in Figure 1 for DJF. This storm track mode characterizes eastward propagation, with significant strength over the Pacific Ocean.

Indeed, as might be expected, the scale and structure of EOF1 in Figure 2a is very similar to the Pacific branch of the second fastest growing instability mode in Figure 9 of Ref. [75] for a climatological January three-dimensional basic state. It also closely resembles the wavetrains in Figure 5 of Ref. [16] for the key point of 35° N and 150° E. As well, it is comparable with the wavetrain in Figure 2c of Ref. [19] based on key point analysis of 300 hPa meridional wind. January EOF3, shown in our Figure 2a, is a synoptic-scale wavetrain that is focused over the North American and Atlantic sector and that is closely reminiscent of the fastest growing instability mode shown in Figure 9 of Frederiksen [75] and the Atlantic branch of the associated second fastest growing mode. It is also quite similar to the wavetrain in Figure 3 of Ref. [16] for the key point of 40° N and 70° W. January EOFs 1 and 3, in Figure 2a, are somewhat more extensive across the Pacific and North American and Atlantic sectors respectively.

The leading EOFs for April closely resemble those for January with some shuffling of order. EOF1 for April in Figure 2b is again a Pacific wavetrain with comparable scale to that of EOF1 for January. The leading EOFs for October are again very similar to those for January and April. October EOF1 (Figure 2d) is a wavetrain focused over the Pacific (like the January and April most dominant EOFs). Again, October EOF1 (Figure 2d) is a typical North American and Atlantic synoptic-scale disturbance.

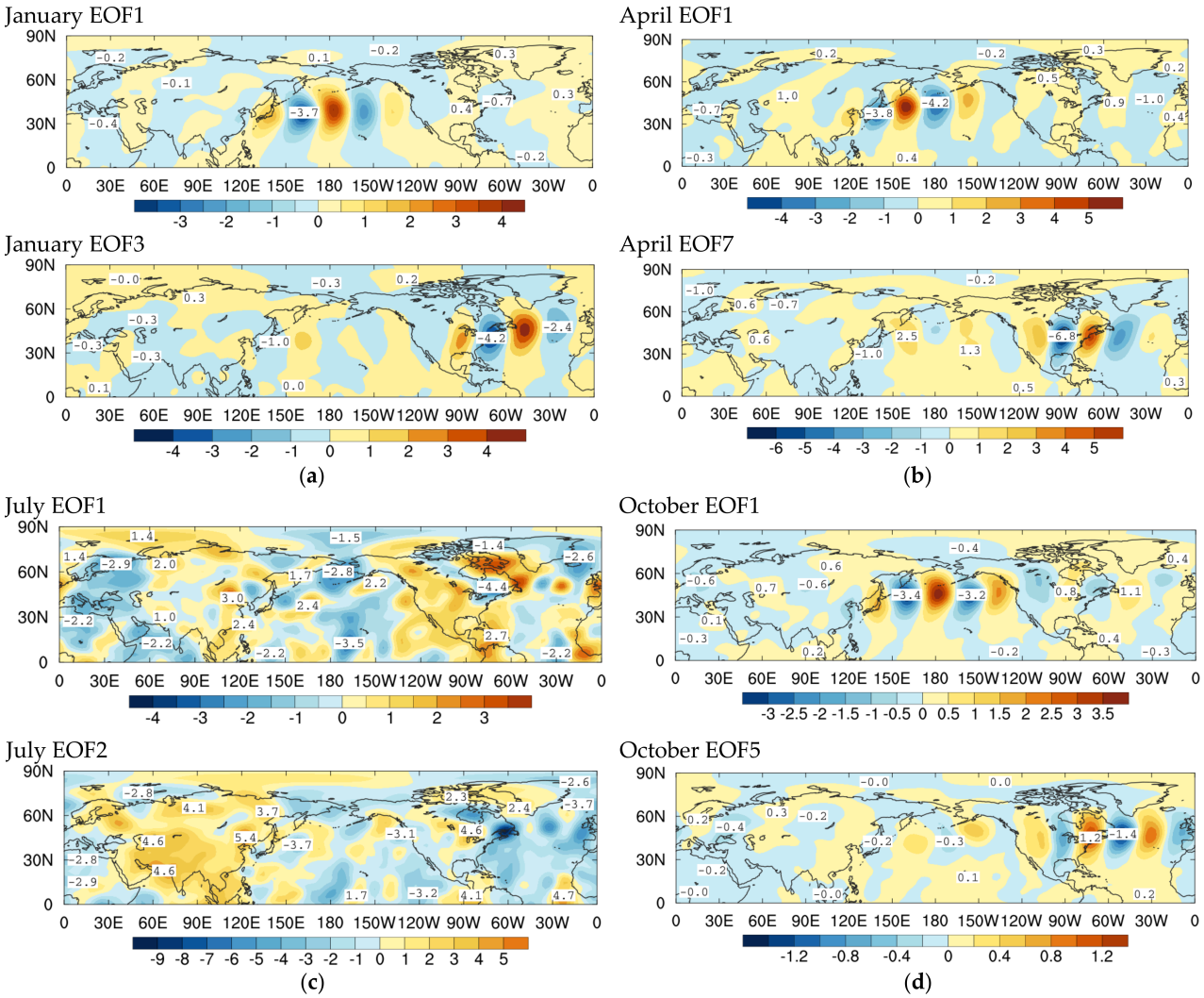

Figure 2. Northern Hemisphere 850 hPa streamfunction of 'standard' EOFs based on all high-pass (period $T_r < 4$ days) synoptic weather fluctuations during 1997 to 2016 in (**a**) January, (**b**) April, (**c**) July and (**d**) October.

As shown in Figure 1, in boreal summer, the 300 hPa jet stream is more zonally extensive with a clear southern branch over the Middle East and Asia, while in the other three seasons, the Pacific and Atlantic branches are more dominant. This and the warmer moist atmosphere with increased diabatic effects (Appendix B) are reflected in the leading EOFs for July shown in Figure 2c. July EOF1 and EOF2 (Figure 2c) have a larger scale wavetrain structure across Africa, the Middle East and Asia, as well as centers over the North American–Atlantic sector, and are somewhat weaker over the Pacific region. In the eastern hemisphere, these EOFs have the typical synoptic-scale wavetrain across North America and the Atlantic seen in the fastest growing July instability mode shown in Figure 13 of Frederiksen [75].

Supplementary Figure S1 show examples of EOFs with more longitudinally extensive wavetrains covering the Pacific sector (January EOF9), the North American–Atlantic sector January EOF11) and both (April EOF3 and 13 and October EOF7). Interestingly, July subdominant EOF14 in Supplement Figure S1c has a very strong and clear Rossby wavetrain across the North American–Atlantic sector like the quasigeostrophic July instability mode in Figure 13 of Ref. [75].

5.2. Band-Pass Filtered Weather Systems with Periods $4 \leq T_r < 8$ *Days*

Standard EOFs based on all fluctuations with periods $4 \leq T_r < 8$ days are examined next. First, cyclone–anticyclone wavetrains with a monopole in the latitudinal direction are analyzed followed by dipole onset-of-blocking modes.

5.2.1. Monopole Cyclone–Anticyclone Wavetrain Modes

The 850 hPa streamfunctions of some of the leading standard EOFs are shown in Figure 3. EOFs for each of the central months of the seasons are depicted (January—Figure 3a; April—Figure 3b; July—Figure 3c; October—Figure 3d). We note the larger scale of the longer period disturbances, although there are still broad similarities with the dominant EOFs for the high-pass filtered fluctuations discussed in Section 5.1.

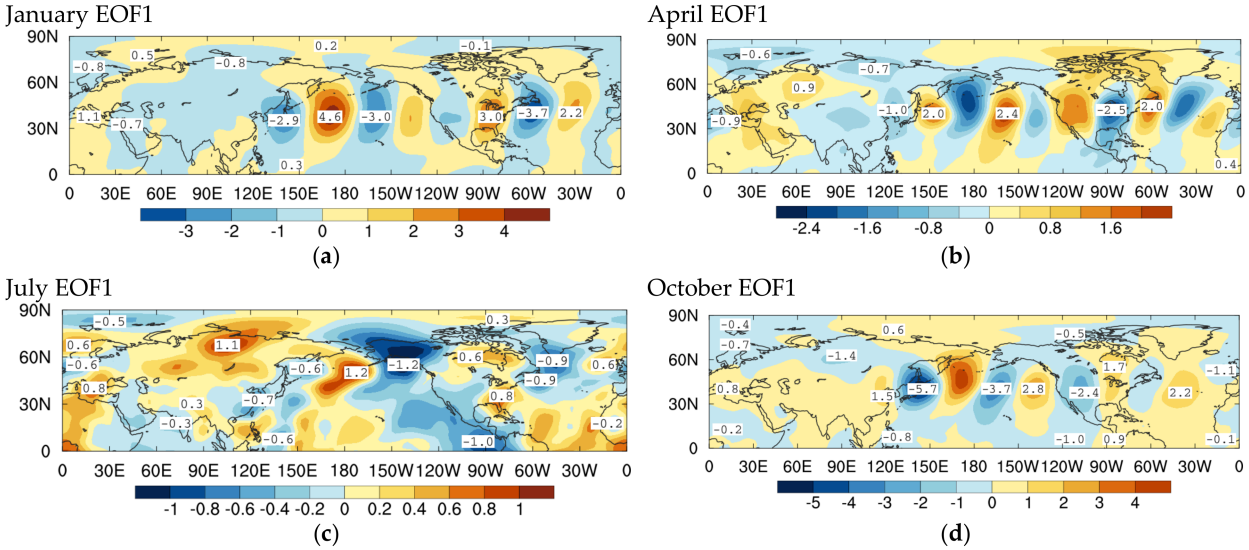

Figure 3. Northern Hemisphere 850 hPa streamfunction of leading 'standard' EOFs based on all band-pass (period $4 \leq T_r < 8$ days) synoptic weather fluctuations during 1997 to 2016 in (**a**) January, (**b**) April, (**c**) July and (**d**) October.

EOF1 for January in Figure 3a is an extensive wavetrain from east Asia across the Pacific, North America and the Atlantic Ocean. It is of larger scale than the January EOFs with period less than 4 days, as expected. EOF1 for April (Figure 3b) again has extensive wavetrains from the western Pacific Ocean to the eastern Atlantic Ocean like the band-pass EOF1 for January. EOF1 for October (Figure 3d) has largest amplitudes on the east coast of Asia and across the Pacific Ocean with diminishing strength across North America and the Atlantic Ocean. July EOF1 has strong centers located over Siberia, across the north Pacific Ocean and extending to North America and the Atlantic Ocean.

Again, there is considerable diversity even amongst the few most dominant EOF patterns, and some of that is shown in Supplementary Figure S2. January EOFs 6 and 9 in Figure S2a again have extensive Rossby wavetrains across the NH. EOF9 is particularly interesting since the wavetrain has large amplitude across the Mediterranean, North Africa and the Middle East where the jet streams in Figure 1a,b for DJF are significant but weaker than over the Pacific and Atlantic Oceans. Such modes likely contribute to the extension of the winter storm track in our Figure 13a across the Mediterranean and the subsidiary peak over the Middle East. In EOFs 4 and 7 for April in Figure S2b, the wavetrain is more localized to the Pacific and North American–Atlantic sectors, respectively, than in main text Figure 3b. EOFs 2 and 3 for October in Figure S2d are respectively focused from the east coast of Asia to the Pacific sector and more extensive from the Pacific to Atlantic regions.

For July, EOFs 6 and 10 show modes strongly focused over the north Pacific Ocean and close to the east Asian coast respectively.

5.2.2. Onset-of-Blocking Dipole Modes

Frederiksen [67] found that instability calculations of NH three-dimensional climatological flows produced baroclinic synoptic-scale disturbances such as the monopole cyclogenesis modes in his Figure 2, with a period of 3.3 days, and as well longer period modes with dipoles in the latitudinal direction. For example, Figure 6 of Frederiksen [67] shows a dipole mode with a period of 6.6 days. Such modes were termed 'onset-of blocking' modes and postulated to start the process of block formation by [67,68]. These baroclinic precursors to the mature block stage were also found in the observational studies of Refs. [57,76–79].

Frederiksen and Webster [80] and Frederiksen [81] review theories of the onset, maturation and maintenance of blocking with Figures 3 and 4 of Ref. [81] showing the good agreement between the onset and maturation theories of Frederiksen [67,68] and the observational study of Dole [76]. The blocking process has also been analyzed from the viewpoint of potential vorticity [82].

Here we again find dipole onset-of-blocking modes amongst the subdominant standard EOFs with periods between 4 to 8 days. They are relatively prevalent during the cooler months with examples shown in Figure 4 where the dipoles occur over the Pacific Ocean upstream and into the region of key centers of the Pacific North American pattern as in the theoretical studies and observations [57,67,68,76–79].

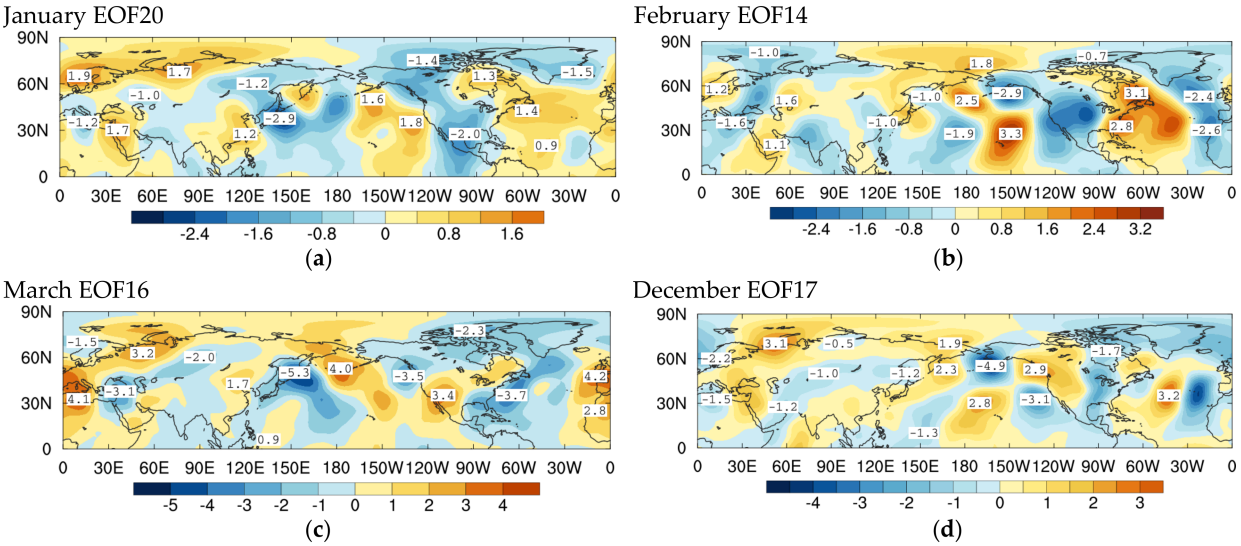

Figure 4. As in Figure 3, for subdominant 'standard' EOFs with dipole structures in (**a**) January, (**b**) February, (**c**) March and (**d**) December..

6. Instability EOFs—Separate Growing Fluctuations

Next, we turn our attention from the 'standard' EOFs based on all fluctuations of weather systems in each frequency band to 'instability' EOFs [53]. As described in Section 3 and Appendices C and D, these are determined by first separating the 6 h evolved anomaly data into bins of growing and decaying disturbances. Thereafter, the EOFs are obtained from the covariance matrices of composites in each of the growth rate bins. We again focus on the leading EOFs of 850 hPa high-pass and band-pass data for the meridional wind ($cos\phi$ weighted) and plot the associated streamfunction fields for the central month of the four seasons.

Throughout this article, we employ the six growth rate bins in Table 1. In our analyses, we concentrate on dominant EOFs corresponding to growing disturbances since they are closely related to rainfall variability as noted in Section 1.3. We note that leading EOFs of disturbances in each decay rate bin are often quite similar to those from the bin with the same growth rate. We shall find it convenient to refer to the three growth rate bins as bins of slow ($0 \leq \omega_i < 0.5$ day^{-1}), moderate ($0.5 \leq \omega_i < 1$ day^{-1}) and fast ($\omega_i \geq 1$ day^{-1}) growing disturbances.

6.1. High-Pass Filtered Weather Systems with Periods $T_r < 4$ Days

As in Section 5, we first discuss the EOFs for high-pass frequency disturbances ($T_r < 4$ days) and then in Section 6.2 consider EOFs for growing band-pass filtered fluctuations ($4 \leq T_r < 8$ days).

6.1.1. Slow Growing Disturbances ($0 \leq \omega_i < 0.5$ Day^{-1})

Figure 5 shows the structures of typical leading EOFs for 6 h evolved high-pass filtered disturbances, with low growth rates ($0 \leq \omega_i < 0.5$ day^{-1}), for January, April, July and October. For January (Figure 5a) synoptic-scale wavetrain structures occur across the Pacific (EOF1), Atlantic (EOF5) and both oceans (EOF3 not shown) as for the standard EOFs in Figure 2a. April Pacific (EOF1) and Atlantic (EOF4) Rossby wavetrains in Figure 5b are very similar to the respective January patterns and with April EOF5 (not shown) extending the Pacific structure across North America. Again, Figure 5d shows that October EOF1 (and EOF3 not shown) is focused in the Pacific storm track and EOF5 in the Atlantic, while EOF11 (not shown) is nearly hemispheric. Many of the leading July EOFs have essentially hemispheric signatures, with EOFs 1 and 7 shown in Figure 5c as examples and in these aspects differ from the standard EOFs.

6.1.2. Moderately Growing Disturbances ($0.5 \leq \omega_i < 1$ Day^{-1})

Next, we analyze moderate growth rate fluctuations with periods less than 4 days and calculate the dominant instability EOFs. Figure 6a shows two of the leading EOFs for January that have close similarities to respective EOFs discussed in Section 6.1.1. but in a different order. EOF1 in Figure 6a is a quite extensive wavetrain from East Asia across the Pacific, North America and the Atlantic Ocean to Europe, with EOF2 (not shown) being more confined to the Pacific sector. EOF3 in Figure 6a is largely a North American and Atlantic sector fluctuation like the January EOF5 in Figure 5a. We also note that the EOFs associated with moderately growing disturbances are displaced slightly equatorward compared with respective EOFs for the slower growing anomalies. This conforms with corresponding findings for Southern Hemisphere storm track modes as described in Ref. [24].

EOFs 1 and 6 shown in Figure 6b for April are similar to EOFs 1 and 3 for January in Figure 6a, respectively, but with the dominant April EOF1 having relatively less amplitude over the Atlantic Ocean. For October, EOF1 in Figure 6d is primarily a Pacific storm track mode but with also some activity over Europe and the Middle East. EOF3 for October (Figure 6d) is interesting in that it is quite extensive with activity across most of the Northern Hemisphere midlatitudes. In the transition seasons, as in winter, the EOFs associated with moderate growth rates track slightly more equatorward than those linked with low growth rates, and there are EOFs that are largely focused in one or the other or both main storm tracks. For July, EOF1 in Figure 6c has large-amplitude wavetrains over the Pacific Ocean and from the Atlantic Ocean across Europe, the Mediterranean and North Africa and the Middle East to Asia. The July EOF4 wavetrain extends across the Atlantic Ocean to Europe and Asia.

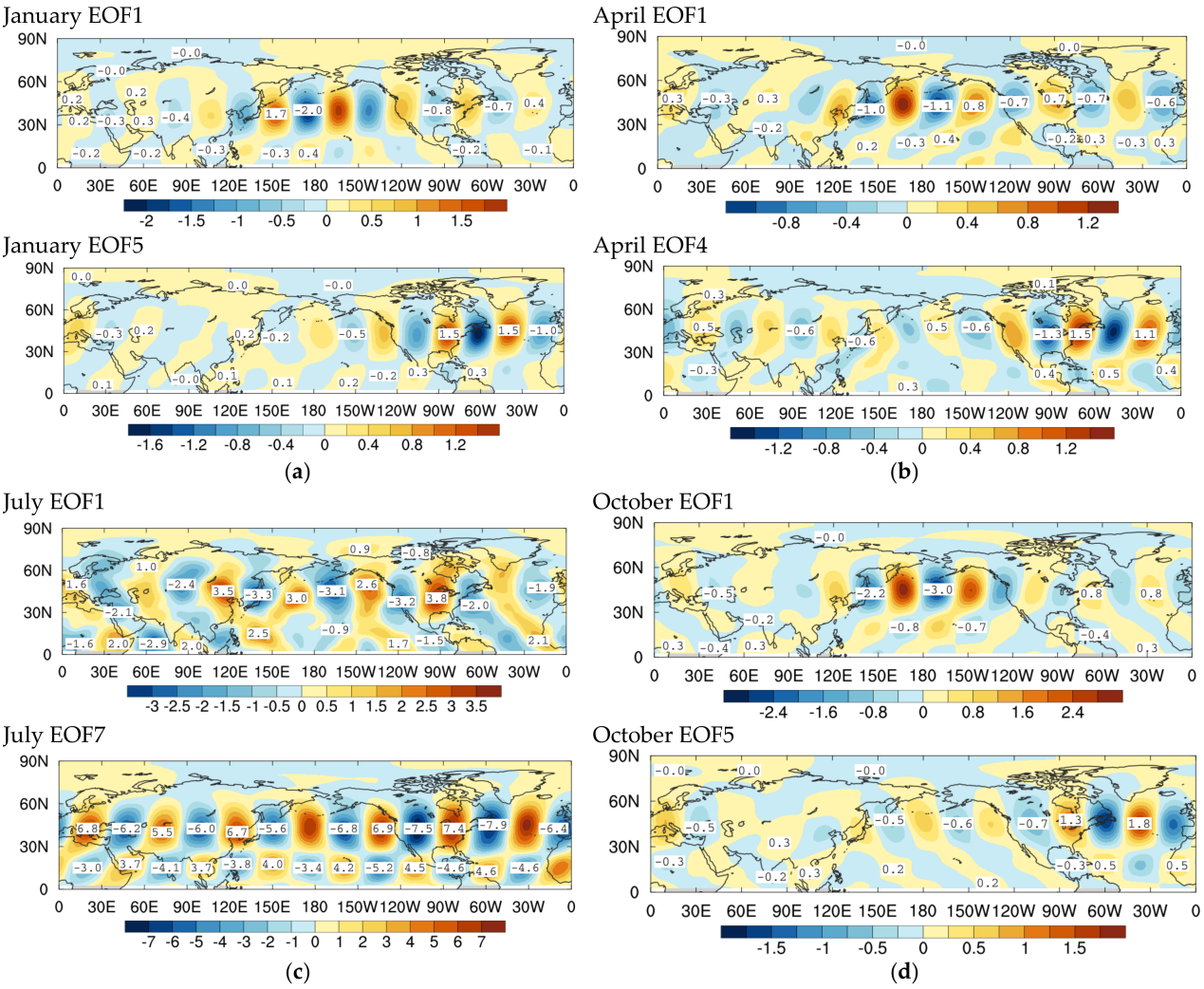

Figure 5. Northern Hemisphere 850 hPa streamfunction of leading 'instability' EOFs for slowly growing ($0 \leq \omega_i < 0.5$ day^{-1}) high-pass filtered (period $T_r <$ 4 days) synoptic weather fluctuations during 1997 to 2016 in (**a**) January, (**b**) April, (**c**) July and (**d**) October.

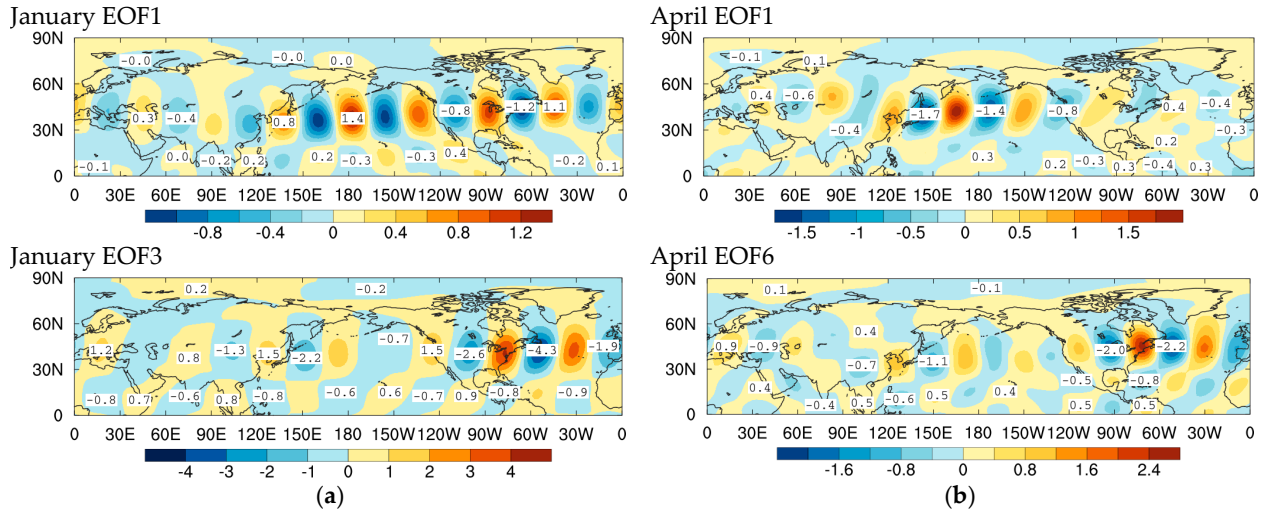

Figure 6. *Cont.*

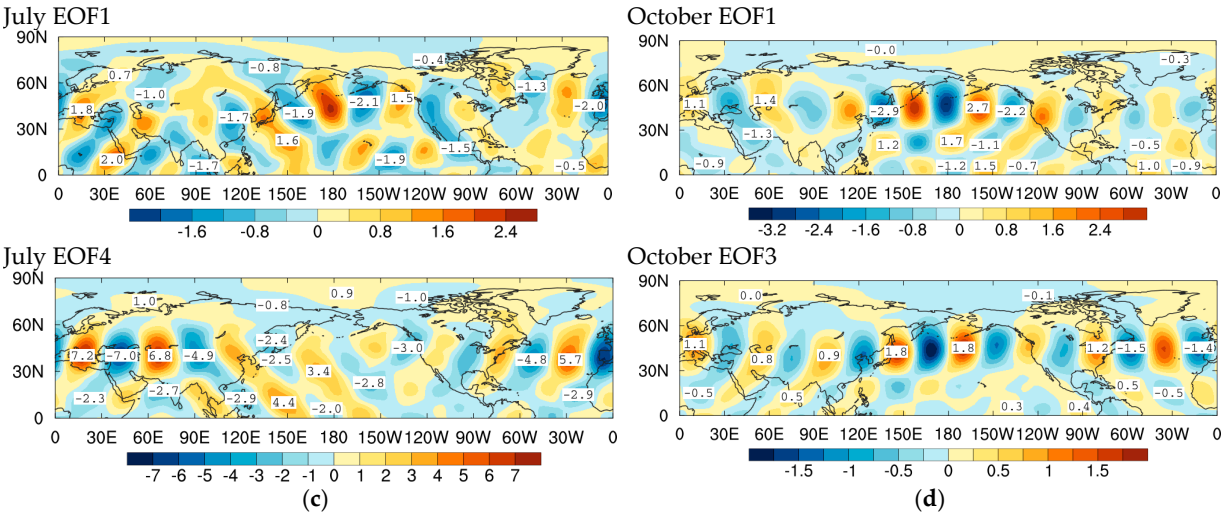

Figure 6. As in Figure 5 for moderately growing disturbances ($0.5 \leq \varpi_i < 1$ day^{-1}) with period $T_r < 4$ days for (**a**) January, (**b**) April, (**c**) July and (**d**) October.

6.1.3. Fast Growing Disturbances ($\varpi_i \geq 1$ Day^{-1})

Lastly, the fast growing high-pass filtered instabilities are examined in this subsection. The changing nature of the structures and amplitudes of the fluctuations in the bin with $\varpi_i \geq 1$ day^{-1} are of particular interest since we expect that they are most likely to be associated with changes in rainfall [59–65]. In particular, in the recent studies of Osbrough and Frederiksen [52,53], explosively growing Southern Hemisphere weather systems were found to be most related to changes in Southern Australian rainfall.

Figure 7a shows the 850 hPa streamfunction of EOFs 1 and 2 for January. The leading EOFs of these explosive weather systems track across the Pacific or North American and Atlantic Ocean regions. They have a southwest to northeast orientation with amplitudes at initiation closer to 30° N to 35° N than the 40° N to 45° N typical of the leading standard EOFs or instability EOFs for slow growing disturbances. EOFs 1 and 5 for April shown in Figure 7b behave in an analogous way with wavetrains across the southern parts of the Pacific and/or North American and Atlantic storm tracks. Again, leading EOFs for October, such as EOF 1 and 2 shown in Figure 7d, have comparable properties to the leading instability EOFs in the bin with $\varpi_i \geq 1$ day^{-1} for January and April. For July, leading EOFs 1 and 4 in Figure 7d reflect the properties of standard July EOFs in Figure 2c with larger scale wavetrains straddling Africa, the Middle East and Asia and crossing the southern parts of North America.

6.1.4. Latitudinal Shifts of EOFs Dependent on the Growth Rate

In this subsection, we have found that the leading EOFs across the Pacific Ocean and North America–Atlantic Ocean basins are generally shifted equatorward, particularly at initiation, for the moderate and fast-growing storm track modes compared with those with low growth rates. This displacement varies somewhat depending on the EOFs and the geographical locations and will be further considered for the statistics based on the STDs in Sections 7 and 8. The equatorward shift with increasing growth rates agrees with the corresponding results for the SH found by Osbrough and Frederiksen [24,53]. Our reasoning is that this is due to the greater instability when moist processes are able to reinforce baroclinic conversions at those latitudes. As discussed in Appendix A and as one can see simply from Phillips' criterion in Equation (A8), for a static stability that is constant with latitude, the $sin^2\phi$ term in the denominator will act to stabilize the flow towards the equator. However, as noted in Appendix B, this can be ameliorated by moist

processes, including an effective moist static stability that decreases sufficiently at the lower latitudes. Indeed, there is overwhelming evidence, some of which is presented there, that diabatic processes play an important role in the generation of explosive cyclones. In particular, the statistical results of Pirret, et al. [83] on the intensity and role of diabatic processes in extratropical storms, initiated over the western Atlantic Ocean and tracking to Northern Europe, resonate with our results. Interestingly, they established that the diabatic contribution, which aids rapid intensification, is substantially correlated with the time spent on the equatorward side of the 300 hPa jet stream in warm moist air.

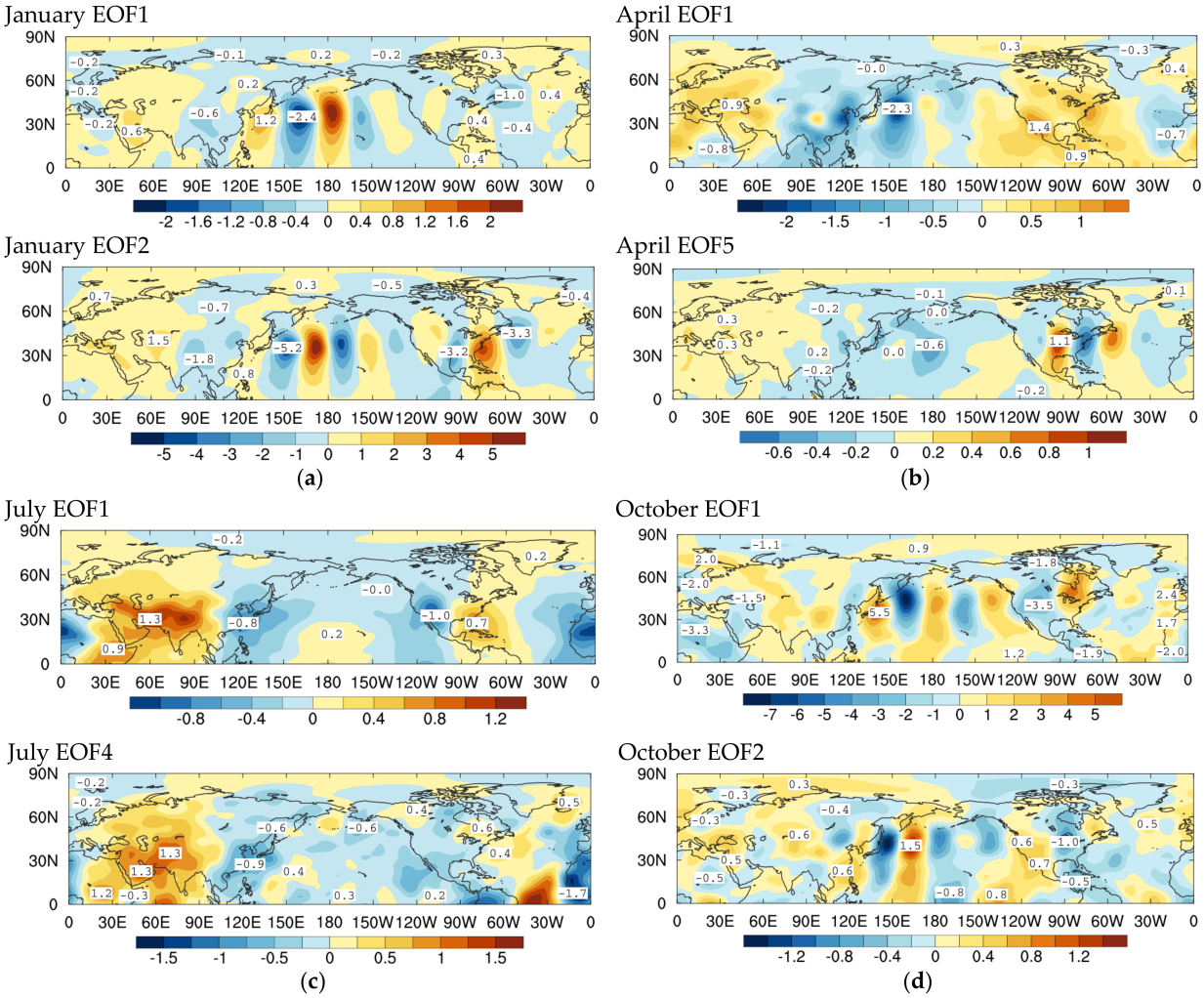

Figure 7. As in Figure 5 for fastest growing disturbances ($\omega_i > 1$ day^{-1}) with period $T_r < 4$ days for (**a**) January, (**b**) April, (**c**) July and (**d**) October.

6.2. Band-Pass Filtered Weather Systems with Periods $4 \leq T_r < 8$ *Days*

In this subsection, 'instability' EOFs are analyzed for band-pass filtered fluctuations ($4 \leq T_r < 8$ days) for the three growth rate bins corresponding to amplifying disturbances. First, monopole cyclone–anticyclone wavetrain EOFs are examined in the three growth rate bins, in Sections 6.2.1–6.2.3. Thereafter, dipole wavetrain EOFs are studied in Section 6.2.4 and related to onset-of-blocking modes.

6.2.1. Slow Growing Monopole Cyclone Wavetrains ($0 \leq \omega_i < 0.5$ Day^{-1})

Figure 8a shows January EOF1, for slow growing disturbances ($0 \leq \omega_i < 0.5$ day^{-1}). It has a streamfunction that is very comparable with the standard EOF1 in Figure 3a. It is again of a larger scale than the high-pass standard EOFs in Figure 2a. The wavetrain

in Figure 8a stretches from the east coast of Asia across all the western hemisphere to Europe. January EOF2 (Figure 8a) is very similar to EOF1 but phase shifted, suggesting that between them they represent orthogonal phases of a travelling mode. Again, there are January EOFs, like EOF6 (not shown), that are essentially hemispheric.

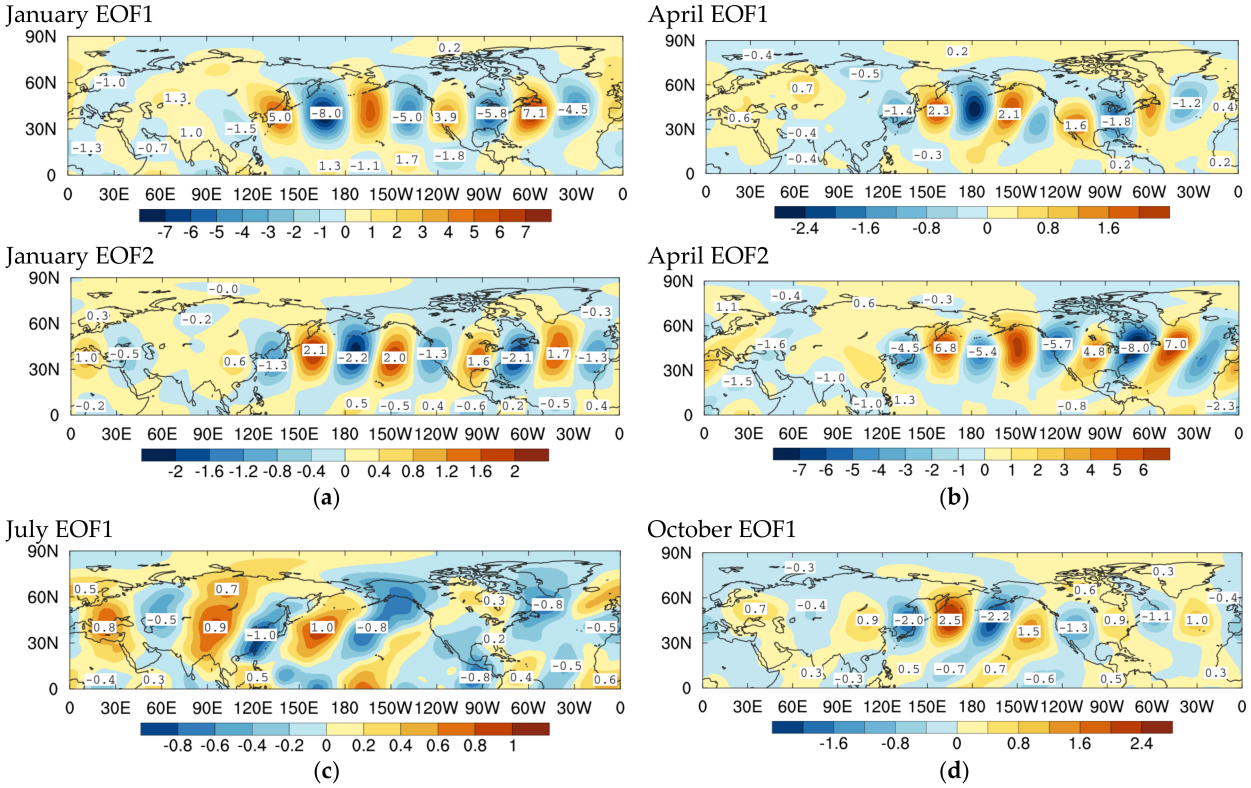

Figure 8. Northern Hemisphere 850 hPa streamfunction of leading 'instability' EOFs for slowly growing ($0 \leq \varpi_i < 0.5$ day^{-1}) band-pass filtered (period $4 \leq T_r < 8$ days) synoptic weather fluctuations during 1997 to 2016 in (**a**) January, (**b**) April, (**c**) July and (**d**) October.

For April, the wavetrains for EOFs 1 and 2 in Figure 8 are quite similar to those for January in Figure 8a and the standard April EOF 1 in Figure 3b. EOF1 for slowly growing disturbances in October in Figure 8d closely matches the standard October EOF1 in Figure 3d with the largest amplitudes across the Pacific Ocean. The dominant EOF1 for July in Figure 8c is an essentially hemispheric wavetrain, while other EOFs, for example EOF3 (not shown), are more localized to the Pacific and North American–Atlantic storm tracks.

6.2.2. Moderately Growing Monopole Cyclone Wavetrain Modes ($\mathbf{0.5 \leq \varpi_i < 1}$ **Day**$^{-1}$)

Figure 9a shows the 850 hPa streamfunctions for January EOF1 based on disturbances in the middle growth rate bin ($0.5 \leq \varpi_i < 1$ day^{-1}). We note that the Rossby wavetrain extends essentially from the east coast of Asia to the Atlantic Ocean, like standard January EOF1 in Figure 3a and EOF1 in Figure 8a, linked to slow growth, but is distinctly displaced towards the southern latitudes. EOF1 for April in Figure 9b is of similar scale and structure to January EOF1 in Figure 9a and similarly displaced equatorward compared with both the standard April EOFs in Figure 3b and the slower growing modes in Figure 8b. The Rossby wavetrain for October EOF1 in Figure 9d is strongest from the east coast of North America, across the Atlantic to Europe and the Middle East. In contrast, October EOF2 (Figure 9d) is focused over the Pacific Ocean, and the equatorward displacement compared with standard October EOF1 in Figure 3d slow growing instability EOF1 in Figure 8d is

again evident. For July, the Rossby wavetrains of EOFs 1 and 2 in Figure 9c are largely hemispheric with EOF1 having a reduced relative amplitude over the Pacific Ocean. Their more southerly location compared with July EOF1 in Figure 8c is again clear.

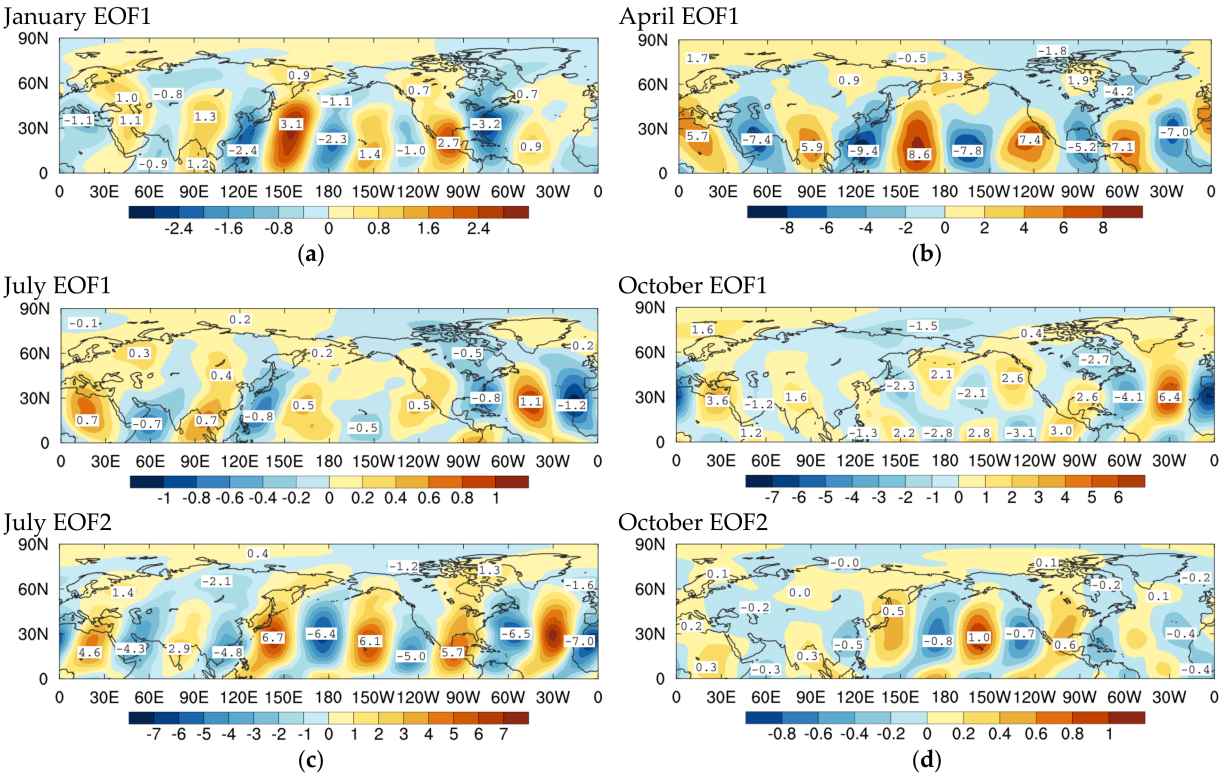

Figure 9. As in Figure 8 for moderately growing disturbances ($0.5 \leq \omega_i < 1$ day^{-1}) for (**a**) January, (**b**) April, (**c**) July and (**d**) October.

Again, the EOFs in Figure 9 based on band-pass filtered transients have larger scale than the corresponding EOFs in Figure 6 for high-pass filtered fluctuations.

6.2.3. Fast Growing Monopole Cyclone Wavetrain Modes ($\omega_i \geq 1$ Day^{-1})

The EOFs of band-pass filtered disturbances in the fastest growth rate bin ($\omega_i \geq 1$ day^{-1}) shown in Figure 10 are of comparable or larger scale to those of a moderate growth rate in Figure 9. They have peak amplitudes near 30° N, which is considerably further equatorward than for the slow growing or standard modes shown in Figures 8 and 3 respectively. Here, we confine our discussion to the dominant EOF1 for each of the four months. However, as for the modes considered earlier in Sections 5 and 6, there are also EOFs for which the Rossby wavetrains are focused over the Pacific Ocean or over the sector between North America and Europe. January EOF1 in Figure 10a is hemispheric in extent with peak amplitudes over the east coast of Asia and the eastern Pacific Ocean. For April, EOF1 has largest amplitudes across the Pacific Ocean and America and over the western Atlantic Ocean, as shown in Figure 10b. The July and October EOFs shown in Figure 10c,d again between them pick up most of the activity centers noted above for January and April. July EOF1 and October EOF1 are again large scale hemispheric wavetrains. As noted in Section 6.1.4 for EOFs of high-pass transients, we again expect that the contributing cause of equatorward shift of EOF Rossby wavetrains for moderately and fast growing band-pass filtered transients is the role of diabatic processes (Appendix B).

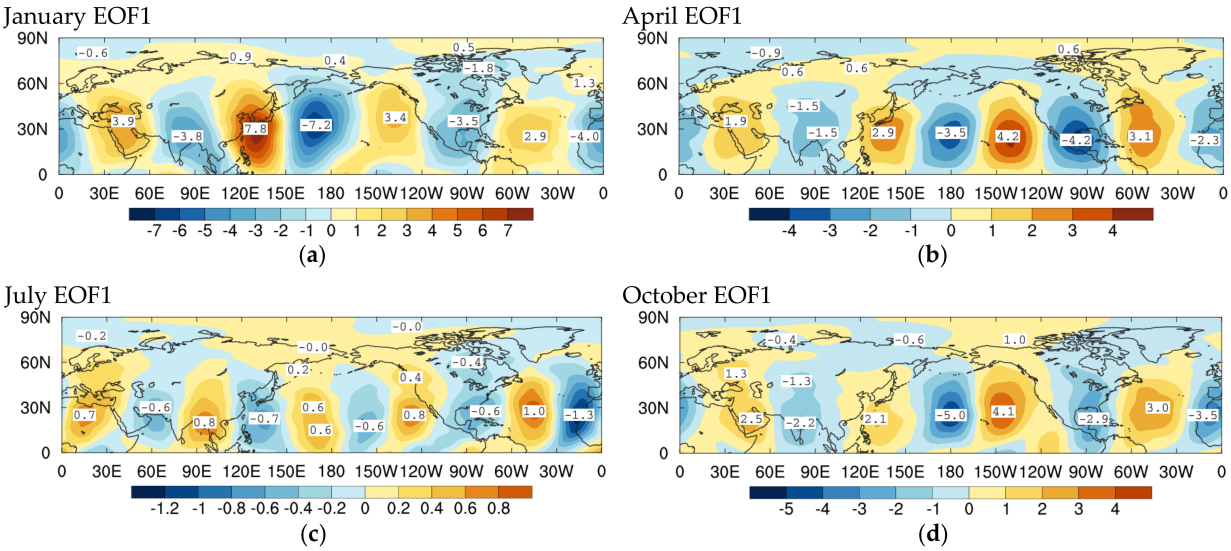

Figure 10. As in Figure 8 for fastest growing disturbances ($\varpi_i > 1$ day^{-1}) for (**a**) January, (**b**) April, (**c**) July and (**d**) October.

6.2.4. Onset-Of Blocking Dipole Modes

In Section 5.2.2, we noted that some of the subdominant standard EOFs for band-pass disturbances consisted of largely dipole modes like the onset-of-blocking modes of Ref. [67]. They can be found throughout the seasonal cycle but tend to be more prevalent during the cooler months. Very similar modes are found for growing disturbances, particularly in the bin of lower growth rates with $0 \leq \varpi_i < 0.5$ day^{-1}, as shown in Figure 11 for typical EOFs in December, January, February and March. We particularly note the dipoles over the Pacific and Atlantic Ocean regions where the mean flow is often diffluent.

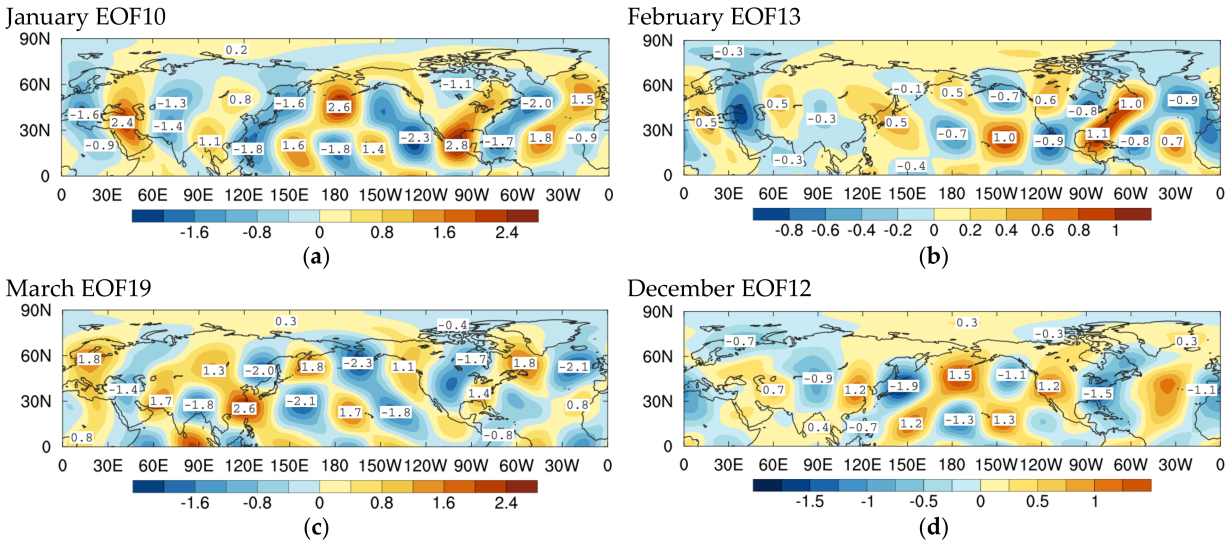

Figure 11. As in Figure 8 for subdominant dipole 'instability' EOFs from slowly growing ($0 \leq \varpi_i < 0.5$ day^{-1}) band-pass filtered (period $4 \leq T_r < 8$ days) synoptic weather fluctuations during 1997 to 2016 in (**a**) January, (**b**) February, (**c**) March and (**d**) December.

Indeed, the leading 20 or so EOFs are primarily monopole cyclogenesis modes apart from some of the standard EOFs of Section 5, with examples in Figure 4, and instability EOFs for the bin for slow growing modes, with examples in Figure 11. The latter result is what one might expect based on the three-dimensional instability theory of blocking and cyclogenesis [67]. It predicts that when the confluent–diffluent basic state is very unstable, cyclogenesis modes are by far the fastest growing and onset-of blocking modes are subdominant. However, for less unstable basic states, while growth rates in general drop, the onset-of-blocking modes are relatively more prominent.

7. Statistics of Weather Systems—All Fluctuations

In this section, we continue our analysis of the statistical properties of the NH storm tracks. We consider here the seasonal variability of the standard deviation (STD) for the 850 hPa streamfunction based on all (growing and decaying) fluctuations for the twenty years of 1997 to 2016. We analyze the high-pass and band-pass filtered disturbances separately. In the subsequent Section 8, the STDs of the separate growing and decaying fluctuations in each of the six growth rate bins shown in Table 1 are then studied. We note that the corresponding results for STDs of meridional wind ($cos\phi$ weighted) (in ms^{-1}) are very similar to those for the streamfunction (in km^2s^{-1}) by multiplying by circa 1.8 (respectively 1.2) for high-pass (respectively band-pass) anomalies.

7.1. Standard Deviations of Weather Systems with Periods $T_r < 4$ *Days*

The standard deviation of the 850 hPa streamfunction anomalies for each season is shown in Figure 12 for filtered high-pass disturbances. In each season, the characteristic Pacific and North American Atlantic storm tracks with centers between 40° N and 55° N are evident, as summarized in Table 2. As well, in boreal summer, strong centers also occur over Northern Africa and between the Middle East and India. The Pacific and Atlantic storm tracks for high-pass disturbances are strongest in DJF, with nearly equal peaks, followed closely by MAM and SON and with far weaker strength in JJA. The peaks of the 700 hPa zonal winds shown in Figure 1 are in reasonable agreement with peaks of main 850 hPa storm tracks, with the caveats of Section 1.5.

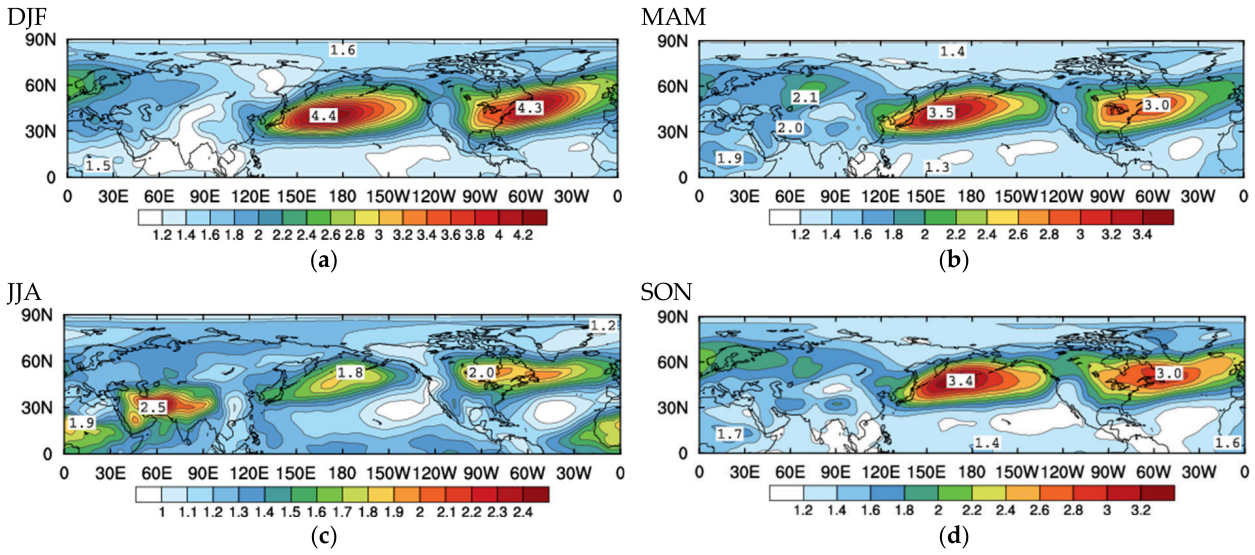

Figure 12. Seasonal variability of standard deviation of Northern Hemisphere 850 hPa streamfunction (km^2s^{-1}), based on all (growing and decaying) high-pass filtered fluctuations (period $T_r < 4$ days) for 1997 to 2016 and for the seasons of (**a**) DJF, (**b**) MAM, (**c**) JJA and (**d**) SON.

Table 2. Seasonal variability of peak values of 850 hPa streamfunction standard deviations (km^2s^{-1}), over the Pacific Ocean and North American–Atlantic sector, with associated latitude, for high-pass results in Figure 12 and band-pass results in Figure 13.

	Pacific	**Pacific**	**North Am-Atlantic**	**North Am-Atlantic**
Season	High-pass	Band-pass	High-pass	Band-pass
DJF	4.4 at 40° N	3.9 at 44° N	4.3 at 46° N	3.9 at 39° N
MAM	3.5 at 40° N	3.7 at 44° N	3.0 at 47° N	3.3 at 44° N
JJA	1.8 at 52° N	2.6 at 48° N	2.0 at 52° N	2.3 at 56° N
SON	3.4 at 48° N	3.4 at 44° N & 50° N	3.0 at 52° N	3.5 at 44° N

For northern winter, the Pacific and North American–Atlantic storm tracks in the band with periods less than 4 days broadly agree with the band-pass results in bands between 2 or 2.5 and 6 days in the data analyses of Blackmon ([9], Figure 5a), Blackmon, et al. ([10], Figures 2b, 3b and 5b), White ([15], Figure 8b) and Hoskins and Hodges ([20], Figures 3a–c and 4a,b). Their results depend somewhat on the vertical level chosen and whether the field is surface pressure, geopotential height or meridional wind as also noted by Blackmon, et al. [10]. However, the locations of the peak strengths of the storm tracks are very similar to the results in our Figure 12a for winter and for spring and autumn in Figure 12b and 12d respectively. For boreal summer (Figure 12c), there is a considerable reduction in the strength of the Pacific and North America–Atlantic storm tracks with a poleward shift in the peaks. This agrees with the results for 500 hPa geopotential height STDs in Figure 9a of Blackmon [9] and for 250 hPa geopotential height in Figure 8a of White [15]. In addition, we see in our streamfunction results for summer, in Figure 12c, a clear storm track across North Africa, with a peak value at 19° N, and the Middle East and Asia, with a central value at 30° N, which is the peak in the whole hemisphere. The latter is only a slight bump in the contours at higher levels in the geopotential height results of Blackmon [9] and White [15], which de-emphasize the subtropics and tropics. These southerly centers are also seen with similar or decreasing strengths in spring and autumn and less so in winter in Figure 12.

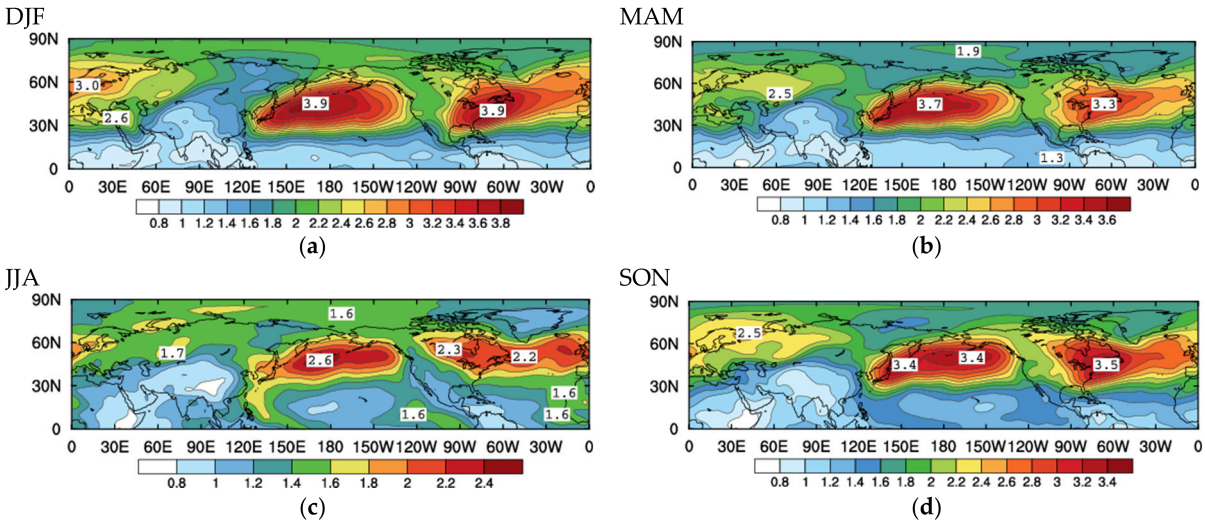

Figure 13. As in Figure 12 for band-pass filtered fluctuations (period $4 \leq T_r < 8$ days) and for the seasons of (**a**) DJF, (**b**) MAM, (**c**) JJA and (**d**) SON.

7.2. Standard Deviations of Weather Systems with Periods $4 \leq T_r < 8$ *Days*

The storm tracks for band-pass filtered 850 hPa streamfunction fluctuations are shown in Figure 13, with central peak values between 39° N and 56° N, as summarized in Table 2. In each season, the latitudinal extents of the Pacific and Atlantic storm tracks in Figure 13 are wider than in Figure 12, which depicts the high-pass results. The storm tracks of the slower propagating larger-scale disturbances also extend with larger amplitudes over northern Europe to Siberia. Again, the strongest Pacific and Atlantic storm tracks occur in DJF, with nearly equal peaks, followed closely by MAM and SON and again with weaker storm tracks in JJA. Again, the summer peaks over the North American–Atlantic region occur at a higher latitude (56° N over North American with a secondary peak at 51° N over the Atlantic) compared with the other seasons. This trend is also the case over the Pacific Ocean, where the summer peak occurs at 48° N, except for autumn where there are two equal peaks at 44° N and 50° N. Interestingly, the summer high-pass local peaks over the Middle East and North Africa in Figure 12c are absent in Figure 13c, and similarly for spring and autumn. However, in winter, there is a clear extension of the North American–Atlantic storm track across to Europe with a peak at 57° N and in the Middle East at 35° N.

These results again have broad similarities, apart from the winter Middle East peak, with those of earlier studies on band-pass filtered disturbances with periods between 2 or 2.5 and 6 days discussed in Section 7.1. However, considering the two bands with $T_r < 4$ days and $4 \leq T_r < 8$ days gives more detailed information on the properties of the synoptic-scale disturbances.

7.3. Relationships Between Streamfunction Standard Deviations and Dynamical Modes of Variability

Ideally, one would like to attribute the causes of the results on the seasonal variability of the streamfunction standard deviations in Figures 12 and 13 and Table 2 to the different dynamical modes of variability operating in the Northern Hemisphere. However, as summarized in our Section 5 and Appendices A and B, the dynamical modes and processes contributing to this variability are numerous and very complex. Indeed, in their review of synoptic-scale weather systems operating in the Northern Hemisphere, Wernli and Gray [84] note "It is challenging to identify cause-effect relations with only diagnostic studies due to the complicated feedback mechanisms involved". Numerical modeling experiments can help, if the models are sufficiently accurate, but Wernli and Gray [84] list five important caveats to the veracity of conclusions based on simulations where different processes are included or excluded. For these reasons, we limit our discussion here to pointing out some consistencies between our findings in this section and the dynamical modes analyzed in Section 5 and Appendices A and B.

In the winter and transition seasons, the Pacific and North American–Atlantic storm tracks in Figures 12 and 13 are closely similar to earlier observational studies based on the geopotential height or meridional wind (Sections 7.1 and 7.2) and to theoretical instability results based on quasi-geostrophic or primitive equation models (Appendix A). Diabatic processes (Appendix B.2) are expected to play a significant role in determining the strength of the variability, as are transitions among tropical, subtropical and extratropical storms (Appendix B.1), but their quantification is in general difficult based on current diagnostic studies [84]. Regional weather systems that affect mainly the subtropics and near equatorial regions are summarized in Appendix B.3 and in the Supplement in Table S1.

In winter, the band-pass results in Figure 13 show considerable amplitude and a distinct center in the Mediterranean to Middle East sector with less strength for the high-pass results. Interestingly, Mediterranean lows, with periods between 3 and 7 days, that largely contribute to the band-pass results also predominantly occur in winter (Appendix B.3). In

summer and the two transition seasons, the high-pass results in Figure 12 show considerable activity over North Africa and across the Middle East and India to China compared with the band-pass findings in Figure 13. We note that most of the synoptic-scale disturbances that affect these regions mainly do so in the warmer seasons and fall into the high-pass frequency band with just a few contributing to both bands (Appendix B.3, Table S1). This is the case for African Easterly Waves and Saharan Depressions that impact on North Africa and Monsoon Depressions, Southwest Vortices and Tropical Easterly Waves that affect parts of the Middle East, India and China.

8. Statistics of Growing and Decaying Weather Systems

Much more detailed information about the structure of NH storm tracks can be obtained by analyzing the Eulerian statistics of synoptic-scale fluctuations in separate growth and decay rate bins. That is the aim in this section where the STDs are calculated for 6-hourly evolved 850 hPa streamfunction fluctuations separated into each of the six growth and decay rate bins in Table 1. These statistics complement the leading instability EOFs presented in Section 6. We again start with the results for high-pass anomalies ($T_r < 4$ days) and follow with band-pass filtered disturbances ($4 \leq T_r < 8$ days).

8.1. Standard Deviations of Weather Systems with Periods $T_r < 4$ Days

The STD of the 6 h evolved NH 850 hPa streamfunction fluctuations with $T_r < 4$ days are shown in Figure 14. The results for the four standard seasons and pertaining to the six growth and decay rate bins (i) to (vi) in Table 1 are shown.

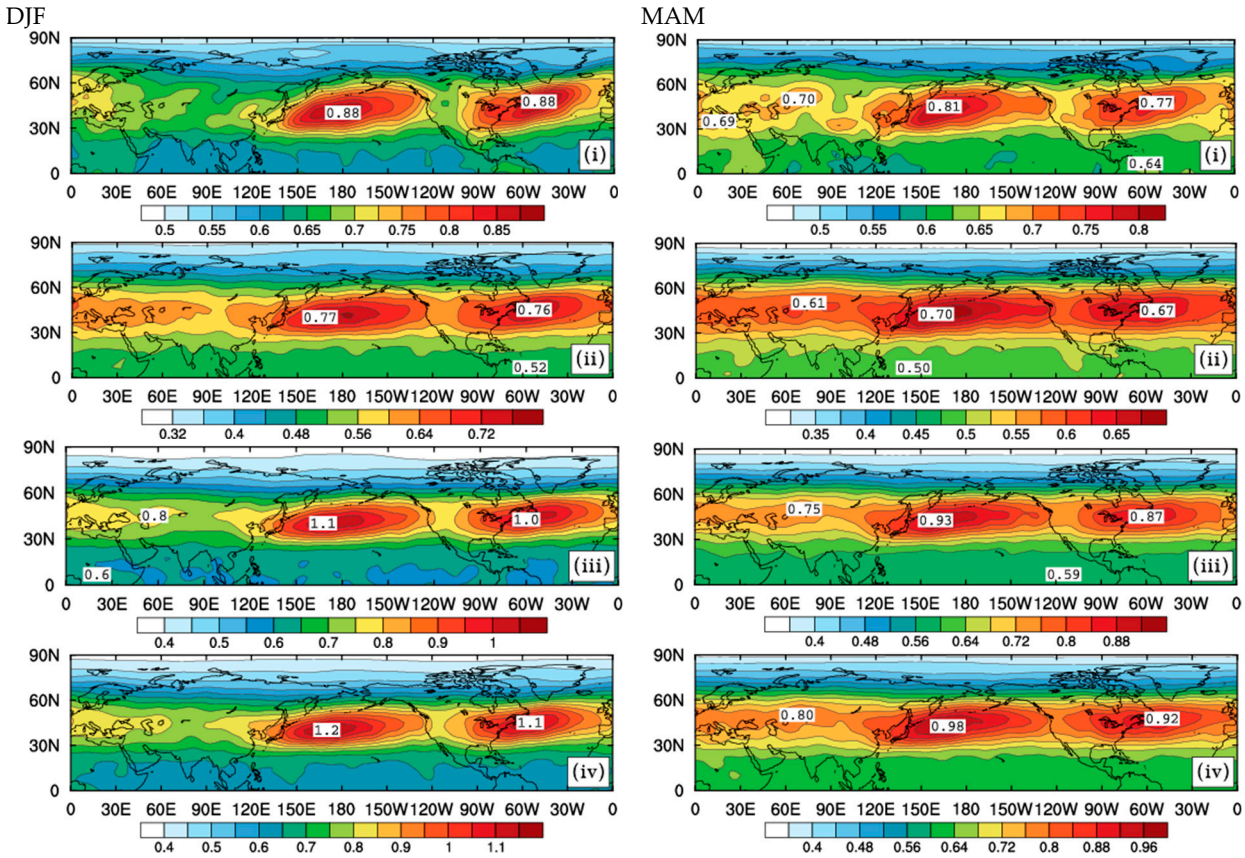

Figure 14. *Cont.*

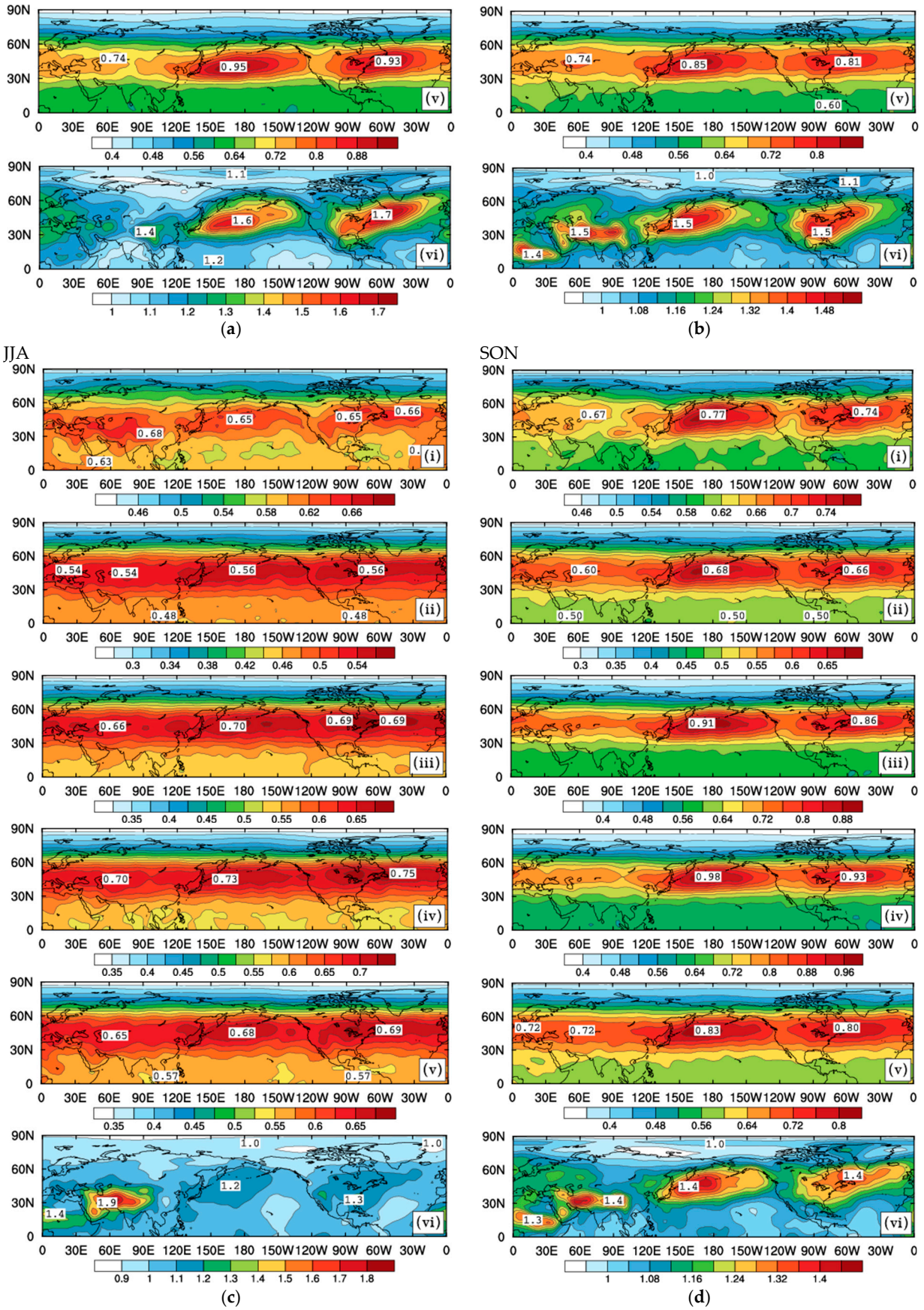

Figure 14. Standard deviation of Northern Hemisphere 850 hPa streamfunction (km^2s^{-1}), for high-pass filtered fluctuations (period $T_r < 4$ days), in decay and growth rate bins (**i**–**vi**) of Table 1. Averages shown for (**a**) winter, (**b**) spring, (**c**) summer and (**d**) autumn during 1997 to 2016.

For DJF, the STDs associated with the explosive growing and decaying disturbances in Figure 14a(vi) and 14a(i) respectively are quite zonally asymmetric, being focused in the Pacific and Atlantic storm tracks between 30° S to 60° S where the 700 hPa zonal winds in Figure 1b for DJF also peak. As well, the explosive storms have subsidiary areas of notable amplitude in the southern zones over North Africa and from the Middle East to India. Interestingly, the STDs in the moderate and slow growth rate and decay rate bins are less zonally asymmetric as might be expected since their growth and decay can be achieved in regions that are less unstable due to lesser roles of baroclinicity and diabatic processes. We also note that the distinct south-west to north-east tilts of the storm tracks for explosive growth in DJF are less evident for the STDs in the other bins. This is a reflection of the more equatorward location of the leading EOFs in the bin with $\varpi_i \geq 1$ day^{-1} as shown in Figure 7a where the wavetrains are also quite localized in the Pacific and Atlantic storm tracks. Perhaps less obvious is the fact that the STDs for moderate growth and decay are slightly broader in the latitudinal direction than for the bin of slower growing disturbances, including on the equatorward flank. Again, this is consistent with the results for the leading EOFs in Figure 5a,b discussed in Section 6. We note the disturbances have evolved for 6 h, which contributes to the fact that the peak STDs for a given growth rate (ϖ_i) bin are larger than those for the same decay rate ($-\varpi_i$ growth rate).

The results described above for the DJF storm tracks for growing and decaying disturbances in the six bins are closely reflected by the corresponding findings for MAM and SON in Figure 14b and 14d respectively. As for the STDs based on all growing and decaying systems in Figure 12, storm tracks for the separate growing and decaying systems are generally slightly weaker in MAM and SON than for DJF in each bin. Interestingly, the explosive storms for MAM and SON in Figure 14c(vi), 14d(vi) also have strong amplitudes over North Africa and from the Middle East to India that rival the peaks in the Pacific and Atlantic storm tracks (consistent with the modes of variability discussed in Section 7.3, Appendix B.3 and Table S1). For MAM the peak STDs of explosive storms are clearly shifted equatorward of those for the slow growing fluctuations over Asia, the Pacific Ocean and the North American–Atlantic sector. For SON, this is also the case over Asia and the Pacific Ocean but not evident over the Atlantic Ocean. However, for both transition seasons, the south-west to north-east tilts of the storm tracks of explosive storms again indicate more southerly initiation of activity.

It is noteworthy from Figure 14c(iv) that for JJA, the strength of the explosive storms over North Africa and from the Middle East to India (Section 7.3, Appendix B.3 and Table S1) are larger than the peaks in the Pacific and Atlantic storm tracks. Peak STDs of explosive storms again occur south of those for slow growing disturbances over Asia and the Atlantic Ocean and with similar locations over the Pacific Ocean. For JJA, the structures of the storm tracks in the other five bins are much more zonally symmetric and weaker, mirroring the much-reduced zonal flows and baroclinicity in JJA shown in Figure 1. It is interesting to compare the results in Figure 14 with those for the corresponding high-pass STDs using the classical analysis method in Figure 12 and see the explosive storms reflected there in the variability based on all fluctuations.

8.2. Standard Deviations of Weather Systems with Periods $4 \leq T_r < 8$ *Days*

Figure 15 shows the same findings as in Figure 14 but for band-pass filtered ($4 \leq T_r < 8$ days) NH 850 hPa streamfunction fluctuations. Again, the results are for 1997 to 2016, and the 6 h evolved anomalies have been stratified by growth rate as shown in Table 1. The generally broader latitudinal extent of the main storm track in Figure 15 compared with Figure 14 of course reflects the larger scale of the longer period weather systems.

Focusing again first on DJF, we see from Figure 15a that the STDs in each of the bins are quite zonally asymmetric with the peak amplitudes in the Pacific and Atlantic storm tracks with the latter from the east coast of North America and extending over Europe. Here, we note a difference between the boreal winter instability mode storm tracks for high-pass and band-pass filtered disturbances compared with the corresponding austral winter storm tracks for the Southern Hemisphere as analyzed by Osbrough and Frederiksen [24]. In the SH study, it was found that the STDs for the high-pass filtered fluctuations were more zonally asymmetric and for the band-pass filtered disturbances the asymmetry was less.

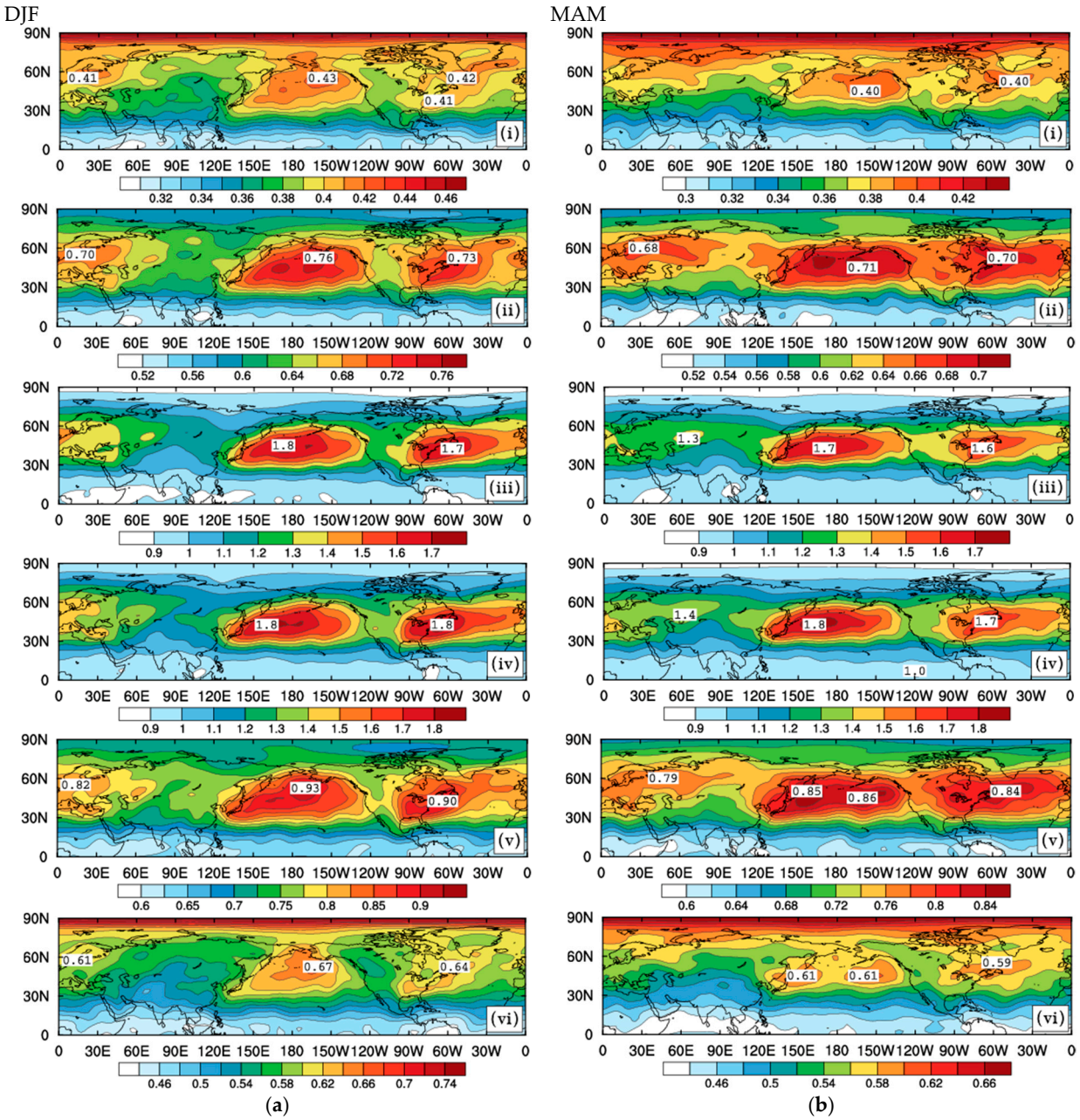

Figure 15. *Cont.*

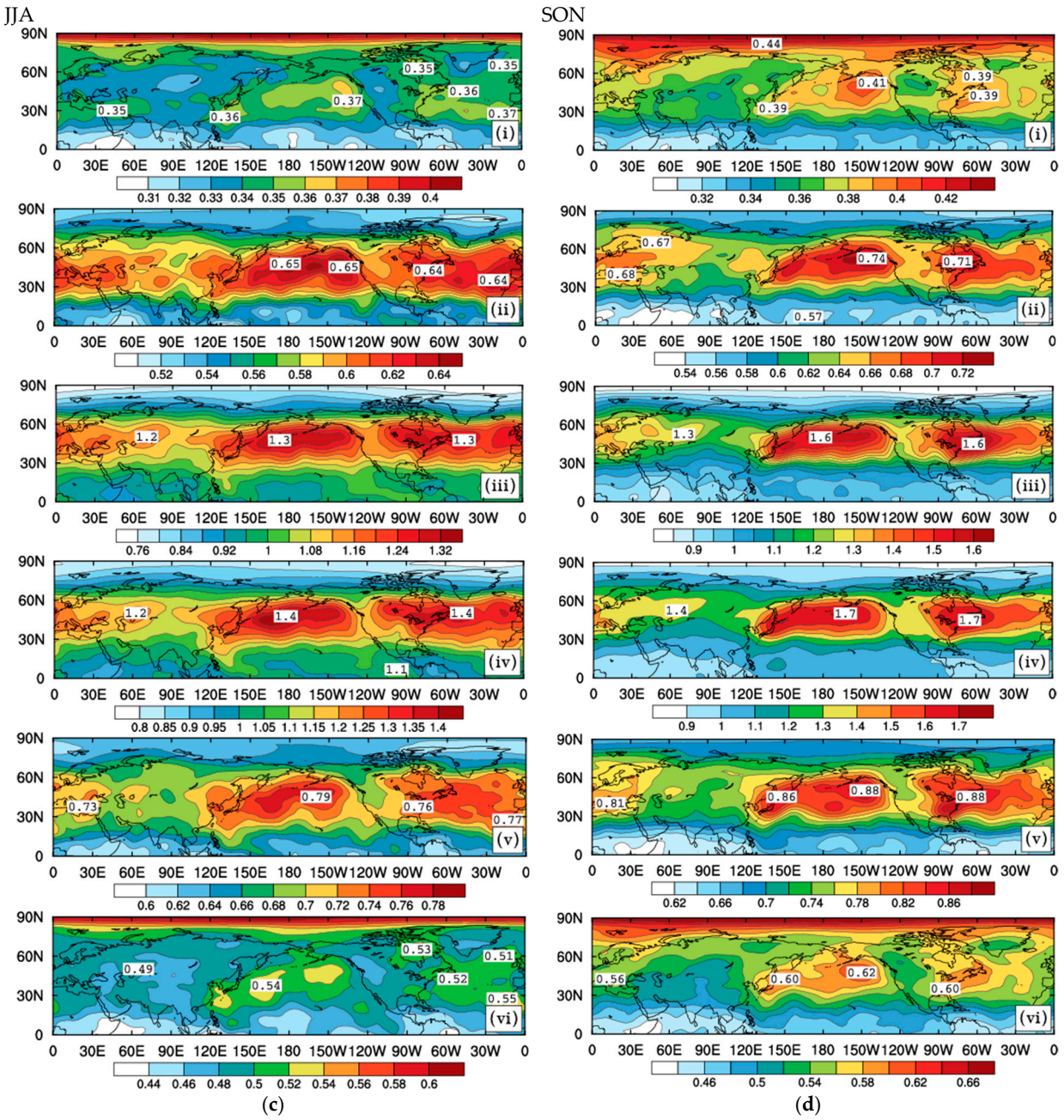

Figure 15. As in Figure 14, but for band-pass filtered anomalies with period $4 \leq T_r < 8$ days and for (**a**) winter, (**b**) spring, (**c**) summer and (**d**) autumn.

The structures of the STDs for MAM and SON, in Figure 15b and 15c respectively, have close likeness to those for DJF with respective peak amplitudes for MAM and SON, slightly less than for DJF for most bins. The reductions in peak values for MAM and SON compared with DJF are particularly notable for the moderately growing disturbances. For these and for the moderately decaying fluctuations, the MAM and SON storm tracks are also less zonally asymmetric. The STDs of the band-pass filtered storm tracks for JJA in Figure 15c are again the weakest for the four seasons and their structures for the bins with slowly and moderately growing and decaying are less localized than for DJF. Again, the structure of the band-pass results for a given growth rate bin are broadly similar to that for the corresponding decay rate bin but of a larger magnitude. The equatorward displacement of the Pacific and Atlantic Ocean band-pass storm tracks for explosive disturbances compared

with the slow growing modes can be seen from the peak STDs for summer and autumn in Figure 15c,d but not for the other seasons.

9. Discussion and Conclusions

Northern Hemisphere synoptic-scale weather systems have been analyzed for the recent 20-year time span of 1997 to 2016, as used by Osbrough and Frederiksen [24] for a SH study. This work has been based on the NNR 6-hourly data described in Section 2. We have related the synoptic wavetrains and structures of the primary storm tracks, based on 850 hPa streamfunctions and $cos\phi$ weighted meridional winds, where ϕ is latitude to the NH jets streams. Two frequency bands of fluctuations have been examined: a high-pass band with period $T_r < 4$ days and a band-pass band with period $4 \leq T_r < 8$ days.

9.1. Standard EOFs and Storm Tracks

First, we have based our work on the familiar ground of 'standard' EOFs and storm tracks determined by the Eulerian variance or STD of all (growing and decaying) fluctuations in a given frequency band. This provides the background for the second more detailed analysis of growing and decaying weather systems associated with three growth rate and three decay rate bins of slow, moderate and fast evolution shown in Table 1. In the dot points below, we summarize our key findings on the seasonal variations of the leading modes of variability based on standard EOFs and the variance of all NH synoptic-scale disturbances. These are as follows:

- Leading EOFs of 850 hPa $cos\phi$ weighted meridional winds and STDs of streamfunctions have peaks between 40° N and 52° N in the main storm track over the Pacific Ocean and North American–Atlantic sector storm tracks in winter and the transition seasons of spring and autumn.
- In summer, these storm tracks are displaced further north with peaks between 48° N and 56° N.
- High-pass activity in summer and the transition seasons also has considerable amplitude over the Mediterranean and North Africa sector and over the Middle East, India and China sector with the peak summer STD occurring over the latter.
- Band-pass EOFs are of a larger scale with broader and wider main storm tracks with the North American–Atlantic activity extending across Europe and into Siberia particularly in winter and the transition seasons; a subsidiary winter branch extends over the Mediterranean and peaks over the Middle East.
- Subdominant band-pass EOFs capture dipole onset-of-blocking modes [67,68], as well as the more typical monopole Rossby wave trains with embedded storms.
- The diagnostics of 850 hPa streamfunctions and $cos\phi$ weighted meridional winds have highlighted the considerable activity in the subtropics. The consistency of the subtropical activity with the important synoptic-scale disturbances that are prevalent in these regions has been noted and analyzed.

9.2. Instability EOFs and Storm Tracks

A major aim of this work has been to use the data-driven methodology developed by Osbrough and Frederiksen [53] in which the 6-hourly NNR data are decomposed spectrally in space and time and the weather systems are analyzed in three growth and three decay rate bins for two filter bands. This has allowed us to study the statistical structures of the growing disturbances in three bins through leading instability EOFs. We have also determined the storm tracks based on STDs of 850 hPa streamfunction anomalies associated with both growing and decaying anomalies in the six bins.

Our key findings on the seasonal variations of instability EOFs and associated storm tracks are as follows:

- Leading EOFs of the slow growing disturbances ($0 \leq \varpi_i < 0.5$ day^{-1}) are generally similar to the standard EOFs, for the respective high-pass and band-pass bands, apart from in summer. Then, they are largely focused in the main Pacific and North American Atlantic storm tracks, as in the other seasons, but of broader longitudinal extent.
- There are subdominant band-pass EOFs for slow growing fluctuations with dipole onset-of blocking modes across the Pacific sector and extending into the Atlantic sector. This is so particularly in the cooler seasons, as for the standard subdominant band-pass EOFs.
- Leading EOFs associated with moderate growth ($0.5 \leq \varpi_i < 1$ day^{-1}), and more so with explosive growth ($\varpi_i \geq 1$ day^{-1}), are generally displaced equatorward compared with corresponding standard EOF and instability EOFs linked to slow growth.
- Leading high-pass summer instability EOFs, linked to explosive growth, exhibit strong activity in the subtropics, including over North Africa, the Middle East, India and China, which is reflected in the standard EOFs.
- The Pacific and North American–Atlantic storm tracks for explosively growing high-pass weather systems are quite localized and have a southwest to northeast orientation. For the other growth and decay bins, the STDs have a zonal symmetric component that increases from winter through spring and autumn to summer, giving a more east to west orientation.
- The storm tracks of explosive high-pass transients also have substantial variance over the Mediterranean and North Africa sector and over the Middle East, India and China sector. The peak summer STDs occurring over the latter sector, as for the standard storm tracks.
- In each season, the storm tracks of the band-pass filtered fluctuations are quite zonally asymmetric with the largest STDs over the Pacific Ocean and in the North American-Atlantic sector. Unlike the case for the high-pass results, this asymmetry persists for the slower and moderately growing and decaying disturbances.
- For both high-pass and band-pass Pacific and North American-Atlantic disturbances, peak STDs for each growth and decay rate bin are weakest in summer and increase to the winter season.

9.3. Conclusions and Future Prospects

We have used the data-driven formulation of Osbrough and Frederiksen [53] to analyze weather systems in two frequency bands and three growth rate and three decay rate bins. This method separates growth from propagation effects and thus is not subject to the risk of apparent deepening of storms due to movement into climatological low-pressure areas [44]. The growth rates and intensity of atmospheric weather systems are calculated directly from the data without assumptions about the large-scale flow fields or static stability unlike complementary theoretical methods (Appendix A) including the commonly used Eady growth rate [6,66]. Stratifying storm track analyses by the growth rate and frequency band is important since changes in rainfall have been found to be particularly affected by changes in high-pass explosive storms [52,53].

We have combined the above methodology with the diagnostics of streamfunction and $cos\phi$ weighted meridional wind, which are more indicative of variability in the subtropics than say geopotential height, to arrive at the findings above. Many of these are new or provide novel insights into established results. As noted by Wernli and Gray [84], the attribution of causes in diagnostic studies is challenging. However, we have noted the consistency of our

results with the processes of baroclinic instability, diabatic processes and tropical–extratropical interactions that contribute to cyclone development in different regions and as well to the modes of variability that act there. Indeed, the evidence of the role of diabatic processes in the generation of explosive storms is overwhelming (Appendices A and B).

The methods that we have used and presented here are quite general and applicable to a vast range of thermodynamical processes with scales from tropical cyclones to convectively coupled equatorial waves, intraseasonal oscillations and teleconnection patterns and to model simulations for weather and climate [80,85] and climate change studies [55,56,70,86,87]. The processes that have traditionally been studied with theoretical models with three-dimensional basic states [80,81] are equally amenable to the approach taken here where the instability properties and intensity are derived directly from the data. In the Northern Hemisphere, further analysis of the instability properties of the many weather types discussed in Appendix B, including subtropical storms, would be worthwhile. Detailed studies of weather systems pertaining to particular regions can also be performed through masking the exterior or using alternative suitable basis functions for the regions. In a sequel to this article, we plan to study how the NH standard storm tracks and their generalization to storm tracks based on the separate growing and decaying components in different growth and decay rate bin have changed over the last seventy years.

Supplementary Materials: The following supporting information can be downloaded at: https://www.mdpi.com/article/10.3390/atmos17050499/s1, Figure S1: Further 'standard' EOFs based on all high-pass (period $T_r < 4$ days) synoptic weather fluctuations; Figure S2: Further 'standard' EOFs based on all band-pass (period $4 \leq T_r < 8$ days) synoptic weather fluctuations; Table S1: Summary of regional synoptic scale weather systems described in main text Appendix B.3.

Author Contributions: Conceptualization, J.S.F. and S.L.O.; methodology, J.S.F. and S.L.O.; software, S.L.O.; validation, J.S.F. and S.L.O.; formal analysis, J.S.F. and S.L.O.; investigation, J.S.F. and S.L.O.; resources, S.L.O.; data curation, S.L.O.; writing—original draft preparation, J.S.F.; writing—review and editing, J.S.F. and S.L.O.; visualization, S.L.O.; supervision, J.S.F.; project administration, S.L.O.; funding acquisition, S.L.O. All authors have read and agreed to the published version of the manuscript.

Funding: This work was supported by the Australian Climate Service. Stacey L. Osbrough is an employee of the Commonwealth Scientific and Industrial Research Organisation. Jorgen S. Frederiksen is Honorary Principal Fellow at the University of Melbourne.

Institutional Review Board Statement: Not applicable.

Informed Consent Statement: Not applicable.

Data Availability Statement: Atmospheric circulation data is available from the NOAA/ESRL website: https://psl.noaa.gov/data/gridded/data.ncep.reanalysis.html (accessed on 7 May 2026). The data displayed in our figures is available upon request.

Acknowledgments: We acknowledge the support of Australian Climate Service.

Conflicts of Interest: The authors declare no conflicts of interest. The funders had no role in the design of the study; in the collection, analyses, or interpretation of data; in the writing of the manuscript; or in the decision to publish the results.

Appendix A. Theories of Extratropical Storm Tracks and Comparisons with Observations

Appendix A.1. Theories and Modeling of Storm Tracks

The early pioneering theories of extratropical cyclogenesis [5–7], based on simple zonal flow basic states on f-planes or beta-planes, sparked further theoretical developments

with more complex models. Baroclinic instability theory was generalized to include both latitudinal and vertical shears, to incorporate the complexity of spherical geometry, to cater for multiple vertical levels and to transition from the quasigeostrophic equations to primitive equations. As well, numerical simulations were performed to study the occlusion process from initial instability modes perturbing zonal mean flows. Reviews of the literature are given in Refs. [80,81,88,89].

The observed transient eddy statistics for both hemispheres, like the large-scale mean flows, are quite asymmetric. Thus, for a theoretical model to explain the relationships between the mean flow structure and the geographical locations of the storm tracks, and eddy statistics, it is necessary to cater to the three-dimensional structure of the mean flow. Interestingly, when this generalization is made, it is found that most of the large-scale disturbances in the atmosphere, from storms to blocks to teleconnection patterns to intraseasonal oscillations and convectively coupled tropical disturbances, have analogues in three-dimensional instability theory [73,80,81,85].

Initially, theoretical models of regional cyclogenesis were made with confluent–diffluent basic states consisting of single planetary waves superimposed on zonally symmetric mean flows by Frederiksen [88]. These instability models were able to capture the relationships between the shapes of the mean flows and the regions of preferential cyclogenesis and associated heat and momentum fluxes. As in observational studies, regions of peak amplitude of cyclogenesis were found slightly downstream and poleward of the locations of maximum vertical shear of the basic state zonal flow. Subsequently, more complex theoretical models with full three-dimensional basic states were developed and for NH, SH and global basic states employing both quasigeostrophic [75,90] and primitive equation [91–93] models in spherical geometry. The results are sensitive to the basic states, the zonal jets and the teleconnection patterns [81,94,95]. These models have also been used for climate change analysis [55,56,70].

Appendix A.2. Comparison of Observational and Theoretical Determinations of Storm Tracks

The cycle of growth, nonlinear saturation or vacillation cycles of extratropical cyclones [81,89,96], with associated changes in structure, is quite complex. It is therefore rather remarkable how well linear baroclinic–barotropic instability theory with three-dimensional basic states can capture the essence of the formation of extratropical storms. As noted in Section 1.4, this theory also captures the core properties of many other large-scale atmospheric disturbances. For example, Sanders and Gyakum [59] noted that their cyclone 'bombs' tended to form downstream and slightly poleward of the associated planetary wave troughs, where the maximum baroclinicity occurs, in agreement with the theory of Frederiksen [88]. Colucci [57,58] noted that explosive cyclogenesis often leads to the formation of blocking, in a process that is consistent with the initial genesis of onset-of-blocking structures, in the theory of Ref. [67], followed by subsequent nonlinear development. The climatological properties of the observed storm tracks in both hemispheres are also broadly consistent with the theoretical developments outlined in Section 1.4 as discussed in many studies [15,27,31,55,64,65,97–99].

Appendix B. Diversity of Weather Systems and the Role of Diabatic Processes

Appendix B.1. Classification of Cyclones

Petterssen and Smebye [100] classified extratropical cyclones into two types: type A cyclones driven by baroclinic instability through low-level thermal advection and type B cyclones that involve the interaction with an upper-tropospheric trough. This was extended by Deveson, et al. [101] and Plant, et al. [102] to include type C cyclones for

which latent heating in the mid-troposphere is important [84,103]. While extratropical storms are cold-core synoptic-scale cyclones that develop primarily through baroclinic conversion, tropical cyclones are warm-core lows that grow through diabatic processes of ocean surface heat fluxes and convection. A further general category is subtropical cyclones, which are hybrids that are driven by both baroclinic instability and diabatic processes and organized convection [84,104,105]. Subtropical cyclones are extratropical lows that develop in the subtropics where diabatic processes are more prevalent due to moister warmer air. They [103] are known by different names in different geographical regions such as east coast lows off the east coast of Australia, Mediterranean cyclones or Medicanes, depending on strength, in the Mediterranean region and Kona lows near Hawaii. Their main features are presented in Table 1 of da Rocha, et al. [104]. Further low-pressure systems are polar lows and cyclones embedded in diabatic Rossby waves [84].

Transitions occur among tropical, subtropical and extratropical cyclones, as summarized in Table 1 of Wood, et al. [105] with the different types characterized in terms of the cyclone phase space parameters of Ref. [106]. The results summarized in Figure 2 of Studholme, et al. [107] suggest a continuum of states among tropical, subtropical and extratropical cyclones. Note that the intensity of extratropical lows resulting from extratropical transition of tropical cyclones may be particularly strong [105,108,109].

Appendix B.2. Diabatic Processes and Explosive Cyclones

Latent heating, in general, increases the growth rate of synoptic-scale baroclinic instabilities. This may be seen from a simple examination of the Phillips' criterion in Equation (A8) or equivalently from an Eady growth rate analysis, with a positive moist static stability that reduces the dry static stability (Wernli and Gray [84] review the literature). Frederiksen and Frederiksen [92] examined the changes in growth rates of atmospheric modes within a primitive equation model with an observed climatological basic state and with and without cumulus convection parameterization. A comparison of their Tables 2 and 3 [92] shows that leading Northern Hemisphere storm track modes increase their growth rates by between 10% and 15% with a realistic moist static stability that is positive, but near criticality, compared with a dry static stability. Growth rates of synoptic-scale storms growing on instantaneous basic states are generally considerably larger, both in model calculations [80] and from data-driven calculations [24,52,53]. This is because the instantaneous potential vorticity gradients are sharper than for climatological basic states. Also, as found by Osbrough and Frederiksen [24,52,53] for the SH and in this study for the NH, the explosive storms tend to be displaced equatorward where the air is warmer and moister.

Grams and Archambault [110] examined the role of diabatic outflow in amplifying Rossby wave trains during the extratropical transition of tropical cyclones over the western North Pacific. They performed numerical experiments to replicate an ensemble of observed extratropical transitions including with and without latent heat release. They found that strong latent heat release is essential for producing a high-amplitude Rossby wave train with intense extratropical lows, as exemplified in their Figure 4. Pirret, et al. [83] studied the role of diabatic processes in the development and intensity of extratropical storms transiting the Atlantic Ocean to Europe. They found that the diabatic processes that contribute to storm intensification were correlated with the time spent on the equatorward side of the 300 hPa jet stream in the warmer moister air.

Appendix B.3. Regional Synoptic Scale Weather Systems

As well as the storms described in the earlier Subsections of the Appendices, there are a number of regional weather systems we need to consider. We summarize here some

of the characteristics of synoptic-scale disturbances that occur across the North African and Mediterranean regions and across the Middle East, India and China. There are large bodies of literature on the properties of these disturbances, with periods between circa 2 to 8 days, and, for the sake of brevity, we summarize here their basic characteristics and refer to recent studies with extensive reviews of the literature. In the Supplement, Table S1 also documents some of the major properties of these weather systems.

Appendix B.3.1. Weather Systems of the North African and Mediterranean Regions

African Easterly Waves are the dominant synoptic-scale disturbances across North Africa with periods between 2 and 5 days and less frequently out to 8 days. They are driven by the baroclinic and barotropic instability of the African Easterly jet and propagate westward including across the north Atlantic Ocean where they frequently initiate Atlantic hurricanes [111–114]. Saharan Depressions form as baroclinic eastward moving disturbances, with periods between 2 and 5 days, when a mid-latitude trough moves southward and interacts with the Saharan heat low [115]. Smaller scale convectively coupled eastward propagating Kelvin waves with periods between about 3 and 7 days and westward propagating Mixed Rossby Gravity waves with similar periods are also triggers of heavy rainfall across North Africa [112,116–118]. As mentioned earlier, eastward propagating Mediterranean cyclones, with periods between 3 and 7 days, significantly influence the weather of these regions, particularly between late autumn and early spring and occasionally become Medicanes with warm cores with heavy precipitation and very strong winds [119–121].

Appendix B.3.2. Weather Systems of the Middle East, India and China

In winter and spring, rain bearing Western Disturbances, which are eastward propagating extratropical cyclones on the subtropical jet, with periods between 3 and 5 days, are the most important synoptic-scale disturbances in the zone across the Middle East, northern India and western China [122]. From early summer to early autumn, rain-bearing Monsoon low pressure systems, with periods between 3 and 6 days, amplify over the Bay of Bengal and track west to northwest across India. The explosive category of these cyclone disturbances are known as Monsoon Depressions that bring heavy downpours over India [123]. In late spring to early autumn, Tibetan Plateau Vortices, which are eastward propagating cyclonic disturbances with periods between 3 and 8 days, develop over the plateau and can cause heavy rainfall over central and southern China [124,125]. To the east of the Tibetan Plateau is the genesis region of eastward propagating intense synoptic-scale systems know as Southwest Vortices, with periods between 2 and 4 days, that often have high impact on southwestern China, during spring and summer, including destructive flash flooding [126]. Just as African Easterly Waves affect the weather and rainfall of North Africa, Tropical Easterly Waves impact southern India and southeast Asia during summer. These tropical waves are westward propagating and have periods between 3 and 6 days. They cause precipitation and can contribute to the genesis of Monsoon Depressions [127].

Appendix C. Method for Extracting Growth Rates from Atmospheric Data

We employ the method developed by Osbrough and Frederiksen [53] for calculating the growing and decaying weather systems and their growth rates directly from atmospheric data described in Section 3. Briefly, the mathematical methodology is as follows. The time dependence of evolving disturbances such as instability modes and POPs is expressed through $\exp(\omega_i - i\omega_r)t$ where ω_r is the angular frequency and ω_i is the growth

rate. To determine the properties of weather systems from data, we again represent the time dependence in the form $\exp -i\varpi(m,n)t$ with

$$\varpi(m,n) = \varpi_r(m,n) + i\varpi_i(m,n). \tag{A1}$$

Here, $\varpi_r(m,n)$ is the angular frequency and $\varpi_i(m,n)$ is the growth rate. Thus, a given spectral component of the streamfunction field has the following form:

$$\Psi_{mn}(t) = \psi_{mn} e^{\varpi_i(m,n)t} e^{-i\varpi_r(m,n)t} \tag{A2}$$

where $\Psi_{mn}(t)$ is presented in Equation (1).

The growth rates and frequencies can then be obtained from knowledge of the streamfunction spectral coefficients at subsequent times. Let Δt denote the time interval between observations, then

$$\left\{ \frac{\Psi_{mn}(t+\Delta t)}{\Psi_{mn}(t)} \right\} = e^{\varpi_i(m,n)\Delta t} e^{-i\varpi_r(m,n)\Delta t}. \tag{A3}$$

Thus, the modulus

$$\left| \frac{\Psi_{mn}(t+\Delta t)}{\Psi_{mn}(t)} \right| = e^{\varpi_i(m,n)\Delta t}, \tag{A4}$$

and the growth rate is given by

$$\varpi_i(m,n) = \frac{1}{\Delta t} ln \left| \frac{\Psi_{mn}(t+\Delta t)}{\Psi_{mn}(t)} \right|. \tag{A5}$$

Similarly, the angular frequency is determined by

$$\varpi_r(m,n) = -\frac{1}{\Delta t} arctan \left[\frac{Im\left(\frac{\Psi_{mn}(t+\Delta t)}{\Psi_{mn}(t)} \right)}{Re\left(\frac{\Psi_{mn}(t+\Delta t)}{\Psi_{mn}(t)} \right)} \right]. \tag{A6}$$

Appendix D. Determination of Empirical Orthogonal Functions

Empirical Orthogonal Functions (EOFs) are defined as the eigenvectors $\boldsymbol{E}$ of the covariance matrix in various spaces including physical and spectral spaces. Suppose the field variable of interest is denoted by $\boldsymbol{x}$ which is a column vector of length N. Then, the EOFs, $\boldsymbol{E}$, are calculated from the following equation:

$$\eta \boldsymbol{E} = < \boldsymbol{x}(t) \boldsymbol{x}^{+}(t) > \boldsymbol{E}. \tag{A7}$$

Here, the values of the eigenvalues η determine the percent variance explained by the eigenvectors $\boldsymbol{E}$ and + denotes the Hermitian conjugate if $\boldsymbol{x}$ are complex spectral components and the transpose for real fields.

Appendix E. Phillips' Criterion for Insipient Baroclinic Instability

The Phillips' Criterion [7] for baroclinic instability of simple zonally symmetric flows is an approximate rule of thumb for incipient storm formation. In spherical geometry, it takes the following form:

$$u^{upper} - u^{lower} - \frac{\sigma b_\kappa c_p cos\phi}{a\Omega sin^2\phi}. \tag{A8}$$

Here, u^{upper} and u^{lower} are suitable zonal winds at the upper and lower pressure levels and σ is the static stability given by the potential temperature difference between these pressure levels. It can include the effects of latent heat release. Also, $a = 6.371 \times 10^6$ m is the earth's radius and $\Omega = 7.292 \times 10^{-5}$ rad s^{-1} its angular rotation speed. The nondimensional

constant $b_\kappa = 0.124$ and $c_p = 1004\ \mathrm{JK^{-1}kg^{-1}}$ is the specific heat of air at constant pressure. The requirement for instability is that the Phillips' Criterion, at a given latitude, ϕ, must be positive.

References

1. Rossby, C.-G. Planetary flow patterns in the atmosphere. *Q. J. R. Meteorol. Soc.* **1940**, *66*, 68–87. [CrossRef]
2. Rossby, C.-G. On the propagation of frequencies and energy in certain types of oceanic and atmospheric waves. *J. Meteorol.* **1945**, *2*, 187–204. [CrossRef]
3. Bjerknes, J.; Solberg, H. Meteorological conditions for the formation of rain. *Geofys. Publ.* **1921**, *2*, 3–61.
4. Bjerknes, J.; Solberg, H. Life cycle of cyclones and the polar front theory of atmospheric circulation. *Geofys. Publ.* **1922**, *3*, 3–18.
5. Charney, J.G. The Dynamics of Long Waves in a Baroclinic Westerly Current. *J. Meteorol.* **1947**, *4*, 135–162. [CrossRef]
6. Eady, E.T. Long Waves and Cyclone Waves. *Tellus* **1949**, *1*, 33–52. [CrossRef]
7. Phillips, N.A. Energy Transformations and Meridional Circulations associated with simple Baroclinic Waves in a two-level, Quasi-geostrophic Model. *Tellus* **1954**, *6*, 273–286. [CrossRef]
8. Sawyer, J.S. Observational Characteristics of Atmospheric Fluctuations with a Time Scale of a Month. *Q. J. R. Meteorol. Soc.* **1970**, *96*, 610–625. [CrossRef]
9. Blackmon, M.L. A Climatological Spectral Study of 500 Mb Geopotential Height of Northern Hemisphere. *J. Atmos. Sci.* **1976**, *33*, 1607–1623. [CrossRef]
10. Blackmon, M.L.; Wallace, J.M.; Lau, N.-C.; Mullen, S.L. An Observational Study of the Northern Hemisphere Wintertime Circulation. *J. Atmos. Sci.* **1977**, *34*, 1040–1053. [CrossRef]
11. Lau, N.-C. On the three-dimensional structure of the observed transient eddy statistics of the Northern Hemisphere wintertime circulation. *J. Atmos. Sci.* **1978**, *35*, 1900–1923. [CrossRef]
12. Lau, N.-C. The observed structure of tropospheric stationary waves and the local balances of vorticity and heat. *J. Atmos. Sci.* **1979**, *36*, 996–1016. [CrossRef]
13. Lau, N.-C.; Wallace, J.M. On the distribution of horizontal transports by transient eddies in the northern hemisphere wintertime circulation. *J. Atmos. Sci.* **1979**, *36*, 1844–1861. [CrossRef]
14. Lau, N.-C.; Oort, A.H. A comparative study of observed Northern Hemisphere circulation statistics based on GFDL and NMC analyses. Part I: The time-mean fields. *Mon. Weather Rev.* **1981**, *109*, 1380–1403. [CrossRef]
15. White, G.H. An Observational Study of the Northern Hemisphere Extratropical Summertime General-Circulation. *J. Atmos. Sci.* **1982**, *39*, 24–40. [CrossRef]
16. Wallace, J.M.; Lim, G.H.; Blackmon, M.L. Relationship between Cyclone Tracks, Anticyclone Tracks and Baroclinic Wave-Guides. *J. Atmos. Sci.* **1988**, *45*, 439–462. [CrossRef]
17. Nakamura, H. Midwinter Suppression of Baroclinic Wave Activity in the Pacific. *J. Atmos. Sci.* **1992**, *49*, 1629–1642. [CrossRef]
18. Chang, E.K.; Yu, D.B. Characteristics of wave packets in the upper troposphere. Part I: Northern Hemisphere winter. *J. Atmos. Sci.* **1999**, *56*, 1708–1728. [CrossRef]
19. Chang, E.K.M. Characteristics of wave packets in the upper troposphere. Part II: Seasonal and hemispheric variations. *J. Atmos. Sci.* **1999**, *56*, 1729–1747. [CrossRef]
20. Hoskins, B.J.; Hodges, K.I. New perspectives on the Northern Hemisphere winter storm tracks. *J. Atmos. Sci.* **2002**, *59*, 1041–1061. [CrossRef]
21. Gibson, J.; Kallberg, P.; Uppala, S.; Hernandez, A.; Nomura, A.; Serrano, E. *ERA Description. ECMWF Re-Analysis Project Report Series 1*; ECMWF: Reading, UK, 1997; Volume 74.
22. Kalnay, E.; Kanamitsu, M.; Kistler, R.; Collins, W.; Deaven, D.; Gandin, L.; Iredell, M.; Saha, S.; White, G.; Woollen, J.; et al. The NCEP/NCAR 40-year reanalysis project. *Bull. Am. Meteorol. Soc.* **1996**, *77*, 437–471. [CrossRef]
23. Schubert, S.; Rood, R.; Park, C.-K.; Wu, C.-Y.; Kondratyeva, Y.; Molod, A.; Takacs, L.; Seablom, M.; Higgins, W. *Technical Report Series on Global Modeling and Data Assimilation*; NASA: Greenbelt, MD, USA, 1995; p. 205.
24. Osbrough, S.L.; Frederiksen, J.S. Seasonal Cycle of Southern Hemisphere Explosive Growth and Decay of Storms. *Atmosphere* **2024**, *15*, 660. [CrossRef]
25. Taljaard, J. Development, distribution and movement of cyclones and anticyclones in the Southern Hemisphere during the IGY. *J. Appl. Meteorol.* **1967**, *6*, 973–987. [CrossRef]
26. Trenberth, K.E. Recent Observed Interdecadal Climate Changes in the Northern-Hemisphere. *Bull. Am. Meteorol. Soc.* **1990**, *71*, 988–993. [CrossRef]
27. Trenberth, K.E. Storm Tracks in the Southern-Hemisphere. *J. Atmos. Sci.* **1991**, *48*, 2159–2178. [CrossRef]
28. Trenberth, K.E.; Mo, K.C. Blocking in the Southern-Hemisphere. *Mon. Weather Rev.* **1985**, *113*, 3–21. [CrossRef]

29. van Loon, H. A climatological study of the atmospheric circulation in the Southern Hemisphere during the IGY, Part I: 1 July 1957–31 March 1958. *J. Appl. Meteorol.* **1965**, *4*, 479–491. [CrossRef]
30. Berbery, E.H.; Vera, C.S. Characteristics of the Southern Hemisphere winter storm track with filtered and unfiltered data. *J. Atmos. Sci.* **1996**, *53*, 468–481. [CrossRef]
31. Nakamura, H.; Shimpo, A. Seasonal variations in the Southern Hemisphere storm tracks and jet streams as revealed in a reanalysis dataset. *J. Clim.* **2004**, *17*, 1828–1844. [CrossRef]
32. Rao, V.B.; Do Carmo, A.; Franchito, S.H. Seasonal variations in the Southern Hemisphere storm tracks and associated wave propagation. *J. Atmos. Sci.* **2002**, *59*, 1029–1040. [CrossRef]
33. Klein, W.H. The frequency of cyclones and anticyclones in relation to the mean circulation. *J. Atmos. Sci.* **1958**, *15*, 98–102. [CrossRef]
34. Murray, R.J.; Simmonds, I. A numerical scheme for tracking cyclone centres from digital data. Part I: Development and operation of the scheme. *Aust. Meteorol. Mag.* **1991**, *39*, 155–166. [CrossRef]
35. Murray, R.J.; Simmonds, I. A numerical scheme for tracking cyclone centres from digital data. Part II: Application to January and July general circulation model simulations. *Aust. Meteorol. Mag.* **1991**, *39*, 167–180. [CrossRef]
36. Hodges, K.I. A general method for tracking analysis and its application to meteorological data. *Mon. Weather Rev.* **1994**, *122*, 2573–2586. [CrossRef]
37. Hodges, K. Adaptive constraints for feature tracking. *Mon. Weather Rev.* **1999**, *127*, 1362–1373. [CrossRef]
38. Lefevre, R.J.; Nielsen-Gammon, J.W. An objective climatology of mobile troughs in the Northern Hemisphere. *Tellus A* **1995**, *47*, 638–655. [CrossRef]
39. Blender, R.; Fraedrich, K.; Lunkeit, F. Identification of cyclone-track regimes in the North Atlantic. *Q. J. R. Meteorol. Soc.* **1997**, *123*, 727–741. [CrossRef]
40. Lim, E.-P.; Simmonds, I. Southern Hemisphere Winter Extratropical Cyclone Characteristics and Vertical Organization Observed with the ERA-40 Data in 1979–2001. *J. Clim.* **2007**, *20*, 2675–2690. [CrossRef]
41. Quinting, J.F.; Catto, J.L.; Reeder, M.J. Synoptic climatology of hybrid cyclones in the Australian region. *Q. J. R. Meteorol. Soc.* **2019**, *145*, 288–302. [CrossRef]
42. Simmonds, I.; Keay, K. Variability of Southern Hemisphere extratropical cyclone behavior, 1958–1997. *J. Clim.* **2000**, *13*, 550–561. [CrossRef]
43. Sinclair, M.R. An Objective Cyclone Climatology for the Southern Hemisphere. *Mon. Weather Rev.* **1994**, *122*, 2239–2256. [CrossRef]
44. Sinclair, M.R. A climatology of cyclogenesis for the Southern Hemisphere. *Mon. Weather Rev.* **1995**, *123*, 1601–1619. [CrossRef]
45. Hoskins, B.J.; Hodges, K.I. A new perspective on Southern Hemisphere storm tracks. *J. Clim.* **2005**, *18*, 4108–4129. [CrossRef]
46. Simmonds, I.; Murray, R.J. Southern extratropical cyclone behavior in ECMWF analyses during the FROST special observing periods. *Weather Forecast.* **1999**, *14*, 878–891. [CrossRef]
47. Wang, X.L.L.; Swail, V.R.; Zwiers, F.W. Climatology and changes of extratropical cyclone activity: Comparison of ERA-40 with NCEP-NCAR reanalysis for 1958–2001. *J. Clim.* **2006**, *19*, 3145–3166. [CrossRef]
48. Barnes, M.A.; King, M.; Reeder, M.; Jakob, C. The dynamics of slow-moving coherent cyclonic potential vorticity anomalies and their links to heavy rainfall over the eastern seaboard of Australia. *Q. J. R. Meteorol. Soc.* **2023**, *149*, 2233–2251. [CrossRef]
49. Zhan, X.Y.; Chen, L. Climatology and Changes in Extratropical Cyclone Activity in the Southern Hemisphere during Austral Winters from 1948 to 2017. *J. Appl. Meteorol. Clim.* **2023**, *62*, 971–983. [CrossRef]
50. Messmer, M.; Simmonds, I. Global analysis of cyclone-induced compound precipitation and wind extreme events. *Weather Clim. Extrem.* **2021**, *32*, 100324. [CrossRef]
51. Allen, J.T.; Pezza, A.B.; Black, M.T. Explosive cyclogenesis: A global climatology comparing multiple reanalyses. *J. Clim.* **2010**, *23*, 6468–6484. [CrossRef]
52. Osbrough, S.L.; Frederiksen, J.S. Interdecadal Variations in the Seasonal Cycle of Explosive Growth of Southern Hemisphere Storms with Impacts on Southern Australian Rainfall. *Atmosphere* **2024**, *15*, 1273. [CrossRef]
53. Osbrough, S.L.; Frederiksen, J.S. Interdecadal changes in Southern Hemisphere winter explosive storms and Southern Australian rainfall. *Clim. Dynam.* **2021**, *56*, 3103–3130. [CrossRef]
54. Nielsen, J.W.; Dole, R.M. A Survey of Extratropical Cyclone Characteristics during Gale. *Mon. Weather Rev.* **1992**, *120*, 1156–1167. [CrossRef]
55. Frederiksen, J.S.; Frederiksen, C.S. Interdecadal changes in southern hemisphere winter storm track modes. *Tellus A* **2007**, *59*, 599–617. [CrossRef]
56. Frederiksen, C.S.; Frederiksen, J.S.; Sisson, J.M.; Osbrough, S.L. Trends and projections of Southern Hemisphere baroclinicity: The role of external forcing and impact on Australian rainfall. *Clim. Dynam.* **2017**, *48*, 3261–3282. [CrossRef]
57. Colucci, S.J. Explosive cyclogenesis and large-scale circulation changes: Implications for atmospheric blocking. *J. Atmos. Sci.* **1985**, *42*, 2701–2717. [CrossRef]

58. Colucci, S.J. Comparative diagnosis of blocking versus nonblocking planetary-scale circulation changes during synoptic-scale cyclogenesis. *J. Atmos. Sci.* **1987**, *44*, 124–139. [CrossRef]
59. Sanders, F.; Gyakum, J.R. Synoptic-Dynamic Climatology of the Bomb. *Mon. Weather Rev.* **1980**, *108*, 1589–1606. [CrossRef]
60. McMurdie, L.A.; Katsaros, K.B. Satellite-derived integrated water vapor and rain intensity patterns: Indicators for rapid cyclogenesis. *Weather Forecast.* **1996**, *11*, 230–245. [CrossRef]
61. Petty, G.W.; Miller, D.K. Satellite Microwave Observations of Precipitation Correlated with Intensification Rate in Extratropical Oceanic Cyclones. *Mon. Weather Rev.* **1995**, *123*, 1904–1911. [CrossRef]
62. Martin, J.E.; Otkin, J.A. The rapid growth and decay of an extratropical cyclone over the central Pacific Ocean. *Weather Forecast.* **2004**, *19*, 358–376. [CrossRef]
63. Roebber, P.J. Statistical-Analysis and Updated Climatology of Explosive Cyclones. *Mon. Weather Rev.* **1984**, *112*, 1577–1589. [CrossRef]
64. Risbey, J.S.; McIntosh, P.C.; Pook, M.J. Synoptic components of rainfall variability and trends in southeast Australia. *Int. J. Climatol.* **2013**, *33*, 2459–2472. [CrossRef]
65. Risbey, J.S.; Pook, M.J.; McIntosh, P.C. Spatial trends in synoptic rainfall in southern Australia. *Geophys. Res. Lett.* **2013**, *40*, 3781–3785. [CrossRef]
66. Pinto, J.G.; Zacharias, S.; Fink, A.H.; Leckebusch, G.C.; Ulbrich, U. Factors contributing to the development of extreme North Atlantic cyclones and their relationship with the NAO. *Clim. Dynam.* **2009**, *32*, 711–737. [CrossRef]
67. Frederiksen, J.S. A Unified 3-Dimensional Instability Theory of the Onset of Blocking and Cyclogenesis. *J. Atmos. Sci.* **1982**, *39*, 969–982. [CrossRef]
68. Frederiksen, J.S. A Unified 3-Dimensional Instability Theory of the Onset of Blocking and Cyclogenesis. 2. Teleconnection Patterns. *J. Atmos. Sci.* **1983**, *40*, 2593–2609. [CrossRef]
69. Frederiksen, J.S.; Osbrough, S.L. Tipping points and changes in Australian climate and extremes. *Climate* **2022**, *10*, 73. [CrossRef]
70. O'Kane, T.J.; Frederiksen, J.S.; Frederiksen, C.S.; Horenko, I. Beyond the first tipping points of Southern Hemisphere climate. *Climate* **2024**, *12*, 81. [CrossRef]
71. Boer, G.J.; Shepherd, T.G. Large-Scale Two-Dimensional Turbulence in the Atmosphere. *J. Atmos. Sci.* **1983**, *40*, 164–184. [CrossRef]
72. Schneidereit, A.; Blender, R.; Fraedrich, K. A radius-depth model for midlatitude cyclones in reanalysis data and simulations. *Q. J. R. Meteorol. Soc.* **2010**, *136*, 50–60. [CrossRef]
73. Frederiksen, J.S.; Lin, H. Tropical-Extratropical Interactions of Intraseasonal Oscillations. *J. Atmos. Sci.* **2013**, *70*, 3180–3197. [CrossRef]
74. Wheeler, M.C.; Hendon, H.H. An all-season real-time multivariate MJO index: Development of an index for monitoring and prediction. *Mon. Weather Rev.* **2004**, *132*, 1917–1932. [CrossRef]
75. Frederiksen, J.S. Disturbances and Eddy Fluxes in Northern Hemisphere Flows—Instability of 3-Dimensional January and July Flows. *J. Atmos. Sci.* **1983**, *40*, 836–855. [CrossRef]
76. Dole, R.M. The life cycles of persistent anomalies and blocking over the North Pacific. In *Advances in Geophysics*; Elsevier: Amsterdam, The Netherlands, 1986; Volume 29, pp. 31–69.
77. Dole, R.M. Life cycles of persistent anomalies. Part I: Evolution of 500 mb height fields. *Mon. Weather Rev.* **1989**, *117*, 177–211. [CrossRef]
78. Dole, R.M.; Black, R.X. Life cycles of persistent anomalies. Part II: The development of persistent negative height anomalies over the North Pacific Ocean. *Mon. Weather Rev.* **1990**, *118*, 824–846. [CrossRef]
79. Evans, K.J.; Black, R.X. Piecewise tendency diagnosis of weather regime transitions. *J. Atmos. Sci.* **2003**, *60*, 1941–1959. [CrossRef]
80. Frederiksen, J.S.; Webster, P.J. Alternative Theories of Atmospheric Teleconnections and Low-Frequency Fluctuations. *Rev. Geophys.* **1988**, *26*, 459–494. [CrossRef]
81. Frederiksen, J.S. Instability Theory and Predictability of Atmospheric Disturbances. In *Frontiers in Turbulence and Coherent Structures*; Denier, J., Frederiksen, J.S., Eds.; World Scientific Publishing: Singapore, 2007; Volume 6, pp. 29–57.
82. Nakamura, N.; Huang, C.S.Y. Local Wave Activity and the Onset of Blocking along a Potential Vorticity Front. *J. Atmos. Sci.* **2017**, *74*, 2341–2362. [CrossRef]
83. Pirret, J.S.R.; Knippertz, P.; Trzeciak, T.M. Drivers for the deepening of severe European windstorms and their impacts on forecast quality. *Q. J. R. Meteorol. Soc.* **2017**, *143*, 309–320. [CrossRef]
84. Wernli, H.; Gray, S.L. The importance of diabatic processes for the dynamics of synoptic-scale extratropical weather systems—A review. *Weather Clim. Dyn.* **2024**, *5*, 1299–1408. [CrossRef]
85. Stan, C.; Straus, D.M.; Frederiksen, J.S.; Lin, H.; Maloney, E.D.; Schumacher, C. Review of tropical-extratropical teleconnections on intraseasonal time scales. *Rev. Geophys.* **2017**, *55*, 902–937. [CrossRef]
86. Chemke, R. Persistent austral winter storm track weakening beyond doubling of CO_2 concentrations. *Nat. Commun.* **2025**, *16*, 1935. [CrossRef]

87. Tarin-Carrasco, P.; Petrova, D.; Chica-Castells, L.; Lukovic, J.; Rodó, X.; Cvijanovic, I. Assessment of Future Precipitation Changes in Mediterranean Climate Regions from CMIP6 Ensemble. *Int. J. Climatol.* **2025**, *45*, e70039. [CrossRef]
88. Frederiksen, J.S. Effects of Long Planetary Waves on the Regions of Cyclogenesis—Linear-Theory. *J. Atmos. Sci.* **1979**, *36*, 195–204. [CrossRef]
89. Frederiksen, J.S. Growth and Vacillation Cycles of Disturbances in Southern-Hemisphere Flows. *J. Atmos. Sci.* **1981**, *38*, 1360–1375. [CrossRef]
90. Frederiksen, J.S. The Geographical Locations of Southern-Hemisphere Storm Tracks—Linear-Theory. *J. Atmos. Sci.* **1985**, *42*, 710–723. [CrossRef]
91. Frederiksen, J.S.; Frederiksen, C.S. Southern-Hemisphere Storm Tracks, Blocking, and Low-Frequency Anomalies in a Primitive Equation Model. *J. Atmos. Sci.* **1993**, *50*, 3148–3163. [CrossRef]
92. Frederiksen, J.S.; Frederiksen, C.S. Monsoon Disturbances, Intraseasonal Oscillations, Teleconnection Patterns, Blocking, and Storm Tracks of the Global Atmosphere during January 1979—Linear-Theory. *J. Atmos. Sci.* **1993**, *50*, 1349–1372. [CrossRef]
93. Frederiksen, C.S.; Frederiksen, J.S. Northern-Hemisphere Storm Tracks and Teleconnection Patterns in Primitive Equation and Quasi-Geostrophic Models. *J. Atmos. Sci.* **1992**, *49*, 1443–1458. [CrossRef]
94. Franzke, C.; Feldstein, S.B. The continuum and dynamics of Northern Hemisphere teleconnection patterns. *J. Atmos. Sci.* **2005**, *62*, 3250–3267. [CrossRef]
95. Risbey, J.S.; O'Kane, T.J.; Monselesan, D.P.; Franzke, C.; Horenko, I. Metastability of Northern Hemisphere Teleconnection Modes. *J. Atmos. Sci.* **2015**, *72*, 35–54. [CrossRef]
96. Simmons, A.J.; Hoskins, B.J. Life-Cycles of Some Non-Linear Baroclinic Waves. *J. Atmos. Sci.* **1978**, *35*, 414–432. [CrossRef]
97. Trenberth, K.E. Seasonality in Southern-Hemisphere Eddy Statistics at 500 Mb. *J. Atmos. Sci.* **1982**, *39*, 2507–2520. [CrossRef]
98. Trenberth, K.E. Observed Southern-Hemisphere Eddy Statistics at 500-Mb—Frequency and Spatial Dependence. *J. Atmos. Sci.* **1981**, *38*, 2585–2605. [CrossRef]
99. Hoskins, B.J.; Valdes, P.J. On the existence of storm-tracks. *J. Atmos. Sci.* **1990**, *47*, 1854–1864. [CrossRef]
100. Petterssen, S.; Smebye, S.J. On the development of Extratropical Cyclones. *Q. J. R. Meteorol. Soc.* **1971**, *97*, 457–482. [CrossRef]
101. Deveson, A.C.L.; Browning, K.A.; Hewson, T.D. A classification of FASTEX cyclones using a height-attributable quasi-geostrophic vertical-motion diagnostic. *Q. J. R. Meteorol. Soc.* **2002**, *128*, 93–117. [CrossRef]
102. Plant, R.S.; Craig, G.C.; Gray, S.L. On a threefold classification of extratropical cyclogenesis. *Q. J. R. Meteorol. Soc.* **2003**, *129*, 2989–3012. [CrossRef]
103. Catto, J.L. Extratropical cyclone classification and its use in climate studies. *Rev. Geophys.* **2016**, *54*, 486–520. [CrossRef]
104. da Rocha, R.P.; Reboita, M.S.; Gozzo, L.F.; Dutra, L.M.M.; de Jesus, E.M. Subtropical cyclones over the oceanic basins: A review. *Ann. N. Y. Acad. Sci.* **2019**, *1436*, 138–156. [CrossRef]
105. Wood, K.; Yanase, W.; Beven, J.; Camargo, S.J.; Courtney, J.B.; Fogarty, C.; Fukuda, J.; Kitabatake, N.; Kucas, M.; McTaggart-Cowan, R.; et al. Phase transitions between tropical, subtropical, and extratropical cyclones: A review from IWTC-10. *Trop. Cyclone Res. Rev.* **2023**, *12*, 294–308. [CrossRef]
106. Hart, R.E. A cyclone phase space derived from thermal wind and thermal asymmetry. *Mon. Weather Rev.* **2003**, *131*, 585–616. [CrossRef]
107. Studholme, J.; Hodges, K.I.; Brierley, C.M. Objective determination of the extratropical transition of tropical cyclones in the Northern Hemisphere. *Tellus A* **2015**, *67*, 24474. [CrossRef]
108. Bieli, M.; Camargo, S.J.; Sobel, A.H.; Evans, J.L.; Hall, T. A Global Climatology of Extratropical Transition. Part II: Statistical Performance of the Cyclone Phase Space. *J. Clim.* **2019**, *32*, 3583–3597. [CrossRef]
109. Bieli, M.; Camargo, S.J.; Sobel, A.H.; Evans, J.L.; Hall, T. A Global Climatology of Extratropical Transition. Part I: Characteristics across Basins. *J. Clim.* **2019**, *32*, 3557–3582. [CrossRef]
110. Grams, C.M.; Archambault, H.M. The Key Role of Diabatic Outflow in Amplifying the Midlatitude Flow: A Representative Case Study of Weather Systems Surrounding Western North Pacific Extratropical Transition. *Mon. Weather Rev.* **2016**, *144*, 3847–3869. [CrossRef]
111. Thorncroft, C.; Hodges, K. African easterly wave variability and its relationship to Atlantic tropical cyclone activity. *J. Clim.* **2001**, *14*, 1166–1179. [CrossRef]
112. Peyrillé, P.; Roehrig, R.; Sanogo, S. Tropical Waves Are Key Drivers of Extreme Precipitation Events in the Central Sahel. *Geophys. Res. Lett.* **2023**, *50*, e2023GL103715. [CrossRef]
113. Akinsanola, A.A.; Adebiyi, A.A.; Bobde, V.; Adeyeri, O.E.; Tamoffo, A.T.; Danso, D.K. Projected changes in African easterly wave activity due to climate change. *Commun. Earth Environ.* **2025**, *6*, 2. [CrossRef]
114. Lawton, Q.A.; Weiser, B.; Majumdar, S.J. On the Interannual Variability of African Easterly Waves and Its Relationship with El Nino-Southern Oscillation. *J. Clim.* **2025**, *38*, 5791–5808. [CrossRef]
115. Rieder, J.C.; Aemisegger, F.; Dente, E.; Armon, M. Meteorological ingredients of heavy precipitation and subsequent lake-filling episodes in the northwestern Sahara. *Hydrol. Earth Syst. Sci.* **2025**, *29*, 1395–1427. [CrossRef]

116. Wheeler, M.; Kiladis, G.N.; Webster, P.J. Large-scale dynamical fields associated with convectively coupled equatorial waves. *J. Atmos. Sci.* **2000**, *57*, 613–640. [CrossRef]
117. Frederiksen, J.S. Genesis of intraseasonal oscillations and equatorial waves. *J. Atmos. Sci.* **2002**, *59*, 2761–2781. [CrossRef]
118. Jonville, T.; Borne, M.; Flamant, C.; Cuesta, J.; Bock, O.; Bosser, P.; Lavaysse, C.; Fink, A.; Knippertz, P. Impact of convectively coupled tropical waves on the composition, vertical structure of the atmosphere, and tropical cyclogenesis in the region of Cabo Verde in September 2021 during the CADDIWA campaign. *Atmos. Chem. Phys.* **2025**, *25*, 9765–9786. [CrossRef]
119. González-Alemán, J.J.; Gaertner, M.A.; Sánchez, E.; Romera, R. Subtropical cyclones near-term projections from an ensemble of regional climate models over the northeastern Atlantic basin. *Int. J. Climatol.* **2018**, *38*, E454–E465. [CrossRef]
120. Givon, Y.; Hess, O.; Flaounas, E.; Catto, J.L.; Sprenger, M.; Raveh-Rubin, S. Process-based classification of Mediterranean cyclones using potential vorticity. *Weather Clim. Dyn.* **2024**, *5*, 133–162. [CrossRef]
121. Doensen, O.; Messmer, M.; Dolores-Tesillos, E.; Raible, C.C. Extreme Mediterranean cyclones under future climate change. *EGUsphere* **2025**, *2025*, 1–29. [CrossRef]
122. Hunt, K.M.R.; Baudouin, J.P.; Turner, A.G.; Dimri, A.P.; Jeelani, G.; Pooja; Chattopadhyay, R.; Cannon, F.; Arulalan, T.; Shekhar, M.S.; et al. Western disturbances and climate variability: A review of recent developments. *Weather Clim. Dyn.* **2025**, *6*, 43–112. [CrossRef]
123. Hunt, K.M.R.; Turner, A.G. Wetter, Weaker, and More Frequent Monsoon Low Pressure Systems in CMIP6 Future Scenarios. *J. Clim.* **2025**, *38*, 7603–7623. [CrossRef]
124. Liu, Q.; Fu, C.B.; Xu, Z.F.; Gan, R.Y. Strong Contributions of Abnormal Vortex Street-Like System in the Tibetan Plateau's Wake to Record-Breaking Strong Rainfall over Southern China in April 2024. *J. Clim.* **2025**, *38*, 6893–6906. [CrossRef]
125. Gan, R.Y.; Huang, G. Northward shift of the Tibetan Plateau vortex street-like system intensifies mid- and late-summer rainfall extremes in Beijing. *Adv. Atmos. Sci.* **2026**, *44*, 1–14. [CrossRef]
126. He, D.; Cao, J. A dataset of Southwest China Vortex events based on deep learning and ERA5 reanalysis data. *Big Earth Data* **2025**, *10*, 685–700. [CrossRef]
127. Du, X.Q.; Chu, J.E.; Jin, F.F.; Cheung, H.M. Global coupled dynamics of tropical easterly waves and tropical cyclone genesis. *npj Clim. Atmos. Sci.* **2025**, *8*, 125. [CrossRef]

Disclaimer/Publisher's Note: The statements, opinions and data contained in all publications are solely those of the individual author(s) and contributor(s) and not of MDPI and/or the editor(s). MDPI and/or the editor(s) disclaim responsibility for any injury to people or property resulting from any ideas, methods, instructions or products referred to in the content.